Composites Part B 252 (2023) 110516

Contents lists available at ScienceDirect

Composites Part B

journal homepage: www.elsevier.com/locate/compositesb

Dendrite growth inhibition in a V_6O_{13} nanorods based non-aqueous Zn-ion battery by a scalable polycarbazole@Carbon nanotubes overlayer

Souvik Naskar [a], Manoranjan Ojha [a], Tapu Raihan Gazi [a], Partha Ghosal [b], Melepurath Deepa [a,*]

[a] Department of Chemistry, Indian Institute of Technology Hyderabad, Kandi, 502284, Sangareddy, Telangana, India
[b] Defence Metallurgical Research Laboratory, Defence Research and Development Organization (DRDO), Hyderabad, 500058, Telangana, India

ARTICLE INFO

Handling Editor: Joong Lee

Keywords:
Vanadium
Polycarbazole
Zn-ion
Battery
Carbon nanotubes

ABSTRACT

Inhibiting the growth of dendrites, one of the most serious issues faced by zinc-ion batteries (ZIBs) is addressed by coating the Zn anode with a layer of poly(carbazole)-carbon nanotubes (PCz@CNTs) composite. The electrically conducting robust composite overlayer ensures that the Zn-deposition during charging cycles is homogeneous and completely free of any fiber-like growth. This is confirmed from the cross-sectional electron microscopy analysis of post-cycled PCz@CNTs@Zn electrode. A vanadium oxide nanorods-porous graphitic flakes (V_6O_{13} NRs@PGFs) composite is used as a cathode. It has a large specific surface area, affording short ion-diffusion distances and many vacant sites thus permitting facile Zn^{2+} ion ingress and egress, is used. A remarkable performance results for the non-aqueous ZIB: V_6O_{13} NRs@PGFs//PCz@CNTs@Zn with a capacity of 286 mAh g^{-1} after 300 cycles at 30 mA g^{-1} (with 98% capacity retention), energy density of ~172 Wh kg^{-1} and a nominal voltage of 1.8 V. It is significantly enhanced compared to its analogous ZIB of V_6O_{13} NRs@PGFs//Zn (193 mAh g^{-1}, and 80% capacity retention). The PCzCNTs overlayer imparts long lifespan with nominal capacity fade, guarantees ultra-safe operation, is cost-effective and also easy to scale-up thus providing a solution that can be adapted to other metal-ion batteries free of dendrites and long term cycling stability.

1. Introduction

To address the burgeoning global energy requirements, intensive research efforts are focussed on developing high performing energy storage devices namely, metal-ion or metal-air batteries (metal: Li, Na, Mg, Al, Zn etc) [1–10]. Among these, zinc ion batteries (ZIBs) have garnered immense scientific attention over the last few years primarily due to the following advantages of zinc (Zn). Zn offers (i) a low reduction potential (−0.76 V *versus* SHE) enabling its use as an anode, (ii) a high theoretical gravimetric and volumetric capacities (819 mAh g^{-1} and 5855 mAh cm^{-3} [11] (iii) enjoys high abundancy, (iv) is eco-friendly, (v) is cheap compared to Na or Li or Mg and (vi) is also relatively easier and safer to handle, store, reuse and dispose off [5, 12–20]. The ZIB architecture, typically comprises of a cathode material capable of storing Zn^{2+} ions by intercalation-deintercalation, a Zn foil anode and a Zn salt based aqueous or non-aqueous electrolyte. A quick literature survey [5,13] reveals that while aqueous ZIBs have been studied exhaustively, non-aqueous ZIBs have been relatively less investigated. High ionic conductivity and low cost of the aqueous electrolyte coupled with good chemical compatibility with cathode allowing easy diffusion of Zn^{2+} ions as well as the Zn anode have been the driving factors [5,13]. However, aqueous ZIBs suffer from serious limitations with regard to their potential for commercial applications.

Firstly, the highly undesirable and competing water reduction and oxidation reactions can occur at the Zn-anode and cathode respectively during ZIB operation, resulting in the evolution of H_2 gas at the anode and liberation of O_2 gas at the cathode. These result in severe and fast capacity fade and low Coulombic efficiency. The reactions are also accompanied by the formation of H^+ and OH^- ions which may irreversibly react with Zn or the cathode material ensuing in the formation of unwanted by-products [21] and affecting the storage performance of the ZIB. Secondly, ease of growth of dendrites on the Zn-anode surface in aqueous ZIBs can result in short circuit. Thirdly, the use of water-based electrolyte also narrows the operational electrochemical potential window of the ZIB thus impacting its' energy density. The aforesaid issues provide the impetus to develop long lasting stable ZIBs based on non-aqueous electrolytes, wherein firstly, the chemical or electrochemical reactions involving water are eliminated. Secondly, due to the high reversibility of zinc plating/stripping, Coulombic efficiency is high in the non-aqueous system.

* Corresponding author.
E-mail address: mdeepa@chy.iith.ac.in (M. Deepa).

https://doi.org/10.1016/j.compositesb.2023.110516
Received 1 November 2022; Received in revised form 28 December 2022; Accepted 6 January 2023
Available online 7 January 2023
1359-8368/© 2023 Elsevier Ltd. All rights reserved.

2D or layered materials are preferred as cathodes for non-aqueous and aqueous ZIBs, owing to the open long channels through which Zn^{2+} ions can easily diffuse into and out of. Vanadium-based oxides are promising cathode materials due to the reversible reactions between vanadium and zinc [14,15,22–40]. Among all vanadium-based oxides, V_6O_{13}, due to its open structure and presence of ample proportions of V^{4+}/V^{5+} mixed valance states that allow ultra-fast charge-discharge is ideal for Zn^{2+} ion storage [41–46].

While these are exciting developments, most of the work done is based on aqueous ZIB configurations, which have poor commercial viability and narrow potential windows. Further, Zn anode dissolution and dendritic growth of Zn on Zn metal plate are also major issues. They occur mainly due to nucleation- and plateau-overpotential, which too cause rapid decline of ZIB performance [47,48]. Thus far, few attempts have been made to overcome the issue of dendritic growth. Few have replaced the host-less zinc metal foil anode with conducting 3D hosts such as CNTs [6,49], zincophilic hosts such as Cu or Sn [50–52]. Some have applied insulating layers such as $CaCO_3$, TiO_2, or ZrO_3 to restrict Zn anode dissolution to some extent [53–55]. Polymers containing polar functional groups such as: C═O, N–H can serve as an ion-oriented layer which can absorb Zn^{2+} ions and orient through the polymer chains to facilitate uniform distribution on Zn metal surface during plating [56–58].

Considering the aforementioned points, here, we have designed a heretofore unreported non-aqueous ZIB system based on V_6O_{13} nanorods (NRs) prepared by a hydrothermal route. The elongated structures allow enhanced uptake of Zn^{2+} ions and maximize capacity and the short diffusion pathways afforded by the nanostructured morphology impart ultra-fast charge-discharge rates. Further, to accommodate the volume expansion and contraction experienced by V_6O_{13} NRs during repetitive Zn^{2+} ion insertion and extraction and to also increase the electronic conductivity of the cathode, a composite of V_6O_{13} NRs was prepared with porous graphitic flakes (PGFs). PGFs were synthesized from a low cost environmentally friendly natural material, i.e., puffed rice. Until now, the V_6O_{13} NRs@PGFs composite has not been employed in a ZIB. The electrolyte was zinc triflate dissolved in acetonitrile, which allowed the safe and reliable operation of the ZIB over a wide voltage window of 1.8 V (~0.2–2.0 V), wider than a ΔV of 1.5 V, which has been the voltage window in a majority of previous reports on ZIBs. The energy density of the cell is defined as $E = ½ C.V^2$, where "C" is the capacity and "V" is the voltage window. A wider voltage window implies a higher energy density for the battery (i.e., the cell can store more energy per unit weight). Further, fabrication of high rating batteries entails connecting multiple cells in combination of series and parallel. A wider voltage window will be helpful to achieve a higher voltage by connecting a lesser number of cells in series leading to lesser weight and a smaller size of the battery.

Apart from the novel cathode composition, the conventional Zn-anode was replaced by a Zn-foil coated with a thin layer of a composite of a conducting polymer (poly(carbazole)) and CNTs (PCz@CNTs). This coating at the anode imparted a long-term cycling stability to the ZIB with the following original architecture: V_6O_{13} NRs@PGFs//PCz@CNTs@Zn. The ZIB exhibited an insignificant capacity decay with cycling and showed no dendritic formation at the Zn anode compared to the analogous V_6O_{13} NRs@PGFs//Zn cell (where dendrite formation and capacity fade were observed), thus highlighting the benefit of the PCz@CNTs coating in enabling the ZIB to deliver a remarkably robust electrochemical performance with potential for even commercial applications.

2. Experimental

2.1. Chemicals

Vanadium pentoxide (V_2O_5, ≥99.0%), oxalic acid ($C_2H_2O_4$, anhydrous ≥99.0%), zinc trifluoromethanesulfonate $Zn(CF_3SO_3)_2$, carbazole (≥95.0% GC), zinc metal foil of 0.25 mm thickness, ammonium persulfate (APS), poly(vinyl pyrrolidone) (PVP, average M_w: 360,000), multi-walled carbon nanotubes (CNTs, O.D. 10–15 nm, I.D. 2–6 nm, length 0.1–10 μm), GF/D borosilicate glass fiber and Whatman filter paper were procured from Sigma-Aldrich and used as such. Poly(vinylidene fluoride) (PVdF, average M_w: 534 000), N-methyl pyrrolidone (NMP), and sodium hydroxide (NaOH) were purchased from Merck. Ultrapure water (resistivity ~ 18.2 MΩ cm) was obtained through a Millipore direct Q3UV system. Stainless steel (SS) foils were procured from Alfa Aesar. Puffed rice was procured locally.

2.2. Synthesis of V_6O_{13} nanorods (NRs) and porous graphitic flakes (PGFs)

V_6O_{13} NRs were synthesized by a hydrothermal method based on a previous report. Oxalic acid and V_2O_5 were taken in 40 mL of water in a 1:1 M ratio. The dispersion was sealed with a parafilm stirred vigorously at 75 °C for 2 h. The color of the dispersion transformed from yellow to blue due to the reduction of V^{5+} species to V^{4+} species. Then this formulation was transferred into a Teflon lined autoclave and heated at 180 °C for 3 h. It was cooled to ambient temperature and the obtained black colored solid was filtered, washed with water and dried at 60 °C in a hot air over for 12 h, and labelled as V_6O_{13} NRs.

Puffed rice was crushed to a fine powder by using a motorized grinder. Then the ensuing powder was annealed at 750 °C in a muffle furnace for 4 h with a ramp rate of 2.5 °C.min^{-1} in air. The as-prepared carbon was chemically activated with NaOH, by taking them in a 1:1 (w/w) ratio in water and stirred continuously for 12 h (usually, for 1 g of carbon, a maximum of 5 mL of water was used). Finally, it was washed with deionized water rigorously to eliminate superfluous NaOH, treated with acetone, dried overnight at 80 °C and the resultant powder was labelled as PGFs and stored in a desiccator.

2.3. Synthesis of polycarbazole (PCz) and PCz@CNTs composite

0.2 g of PVP was dissolved in 20 mL of ethanol and 0.1672 g of carbazole monomer was added to the mixture under continuous stirring. When the mixture solution turned transparent, 15 mL of an aqueous solution of 1 M APS was added. Simultaneously, the color of the solution turned milky. While stirring for 10 min, the solution was loaded into a 50 mL Teflon-lined stainless-steel autoclave, which was sealed immediately and maintained at 180 °C for 24 h. Then, the products were cooled to the room temperature, centrifuged, washed with distilled water and ethanol for several times, and finally dried in a vacuum oven at 60 °C for 24 h [59]. 50 mg of PCz and 50 mg of multi-walled CNTs were mixed and ground well using a mortar-pestle. The composite was sonicated in 100 mL of acetonitrile for several hours. Two drops of this suspension were drop-cast on the circular zinc foil and dried at 80 °C for 12 h, and this coating is referred to as PCz@CNTs.

2.4. Fabrication of non-aqueous ZIBs

V_6O_{13} NRs, PGFs, CB and PVdF were taken in the following weight ratios separately: 80:0:10:10, 60:20:10:10. V_6O_{13} NRs and PGFs were composited by ball-milling technique operated at 350 rpm for 5 h. A planetary ball milling instrument (AI-VPB model) equipped with a zirconia jar and zirconia balls were used to grind and make the composites in pre-defined weight ratios. The composite or NRs were then mixed with CB and PVdF and the mixture was ground well using a mortar-pestle assembly independently. Two separate thick slurries were prepared by using 0.2 mL of N-methyl pyrrolidone (NMP) in each case. They were coated immediately on circular stainless steel (SS) electrodes (diameter: 1.5 cm) with the assistance of an overhead projector plastic sheet. The coated SS electrodes were vacuum dried for 12 h at 60 °C. These electrodes are labelled as cathodes and due care was taken to ensure that the masses of the loaded materials were maintained in the

range of 1.5–2 g cm^{-2} in each case. Pristine circular Zn metal foil (diameter: 1.5 cm) and the same foil coated with the PCz@CNTs composite was used as anode for comparative studies. About 3 to 4 drops of an organic electrolyte solution of 0.5 M $Zn(CF_3SO_3)_2$ in acetonitrile were applied over the GF/D borosilicate glass fiber separator, which were cut into circular disks of ~1.6 cm diameter using the electrode cutter. For all cells, this separator/electrolyte assembly was sandwiched between the pristine V_6O_{13} NRs or V_6O_{13} NRs/PGFs (3:1) composite-based cathodes and the Zn- or PCz@CNTs@Zn-anodes. ZIBs were fabricated inside an argon filled MBraun Labstar glove box operating at O_2 and moisture levels of 0.5 and 0.5 ppm respectively. Swagelok cells were employed for ZIB fabrication. Scheme 1 provides the synthetic methodology for the materials and the full cell.

2.5. Instrumental techniques

An Arbin instruments BT-2000 battery tester was employed for galvanostatic charge-discharge (GCD) measurements. An Autolab PGSTAT 302 N potentiostat/galvanostat, having a NOVA 1.9 software, and a frequency response analyzer (FRA) was employed for cyclic voltammetry (CV), linear sweep voltammetry (I–V) and electrochemical impedance spectroscopy (EIS) measurements. For EIS, an input ac sinusoidal voltage of 20 mV was superimposed over the open-circuit dc voltage of the cell, and spectra were recorded over a frequency range of 1 MHz to 0.01 Hz. A PANalytical, X'PertPRO X-ray diffractometer with a Cu-Kα (λ = 1.5406 Å) radiation as the X-ray source was employed for recording XRD patterns of active materials. A Bruker Senterra dispersive micro-Raman spectrometer with a 532 nm laser was used for collecting Raman spectra of active materials. A field emission-scanning electron microscope (FE-SEM, JEOL-JSM-7800) was used to study the surface morphology of electrode materials. X-ray photoelectron spectra (XPS) were obtained on an Axis Supra K-ALPHA surface analysis spectrometer having a monochromatic, micro-focused Al-Kα radiation of 1486.6 eV energy. The base pressure was maintained at ~5×10^{-11} Torr. Pass energies of 160 and 80 eV were employed for acquiring survey and core level spectra with resolutions of 1 and 0.1 eV. Core level spectra were deconvoluted using a non-linear iterative least-squares Gaussian-Lorentzian fitting protocol with the help of a Jandel Peak FitTM (version 4.01) program. Corrections due to charging effects were taken care of by using C(1s) as an internal reference and the Fermi edge of a gold sample. A JEOL 2100 transmission electron microscope (TEM) operating at an accelerating voltage of 200 kV was used to study the microstructure of active materials. Samples were coated over carbon-coated copper grids by first dispersing them in acetone followed by their application over the grid and then used after solvent evaporation. Atomic force microscopy (AFM) topography images were recorded on a Bruker, Multimode 8 microscope using etched silicon probes and the analysis was carried out using a NanoScope analysis application. Fourier transform infrared (FTIR) spectrum of PCz was recorded on a Jasco FT/IR-4600 machine.

3. Results and discussion

3.1. Microstructural and electrical properties of cathode materials

FE-SEM images of V_6O_{13} NRs in Fig. 1a reveals the highly monodisperse nature of the rods achieved over length scales of tens of microns. Clusters of densely packed nanorods oriented along different directions are visible. High magnification images in Fig. 1b and c shows that the rods are about 300–400 nm in length and have diameters in the range of 50–60 nm, and they also tend to aggregate. Irregular shaped

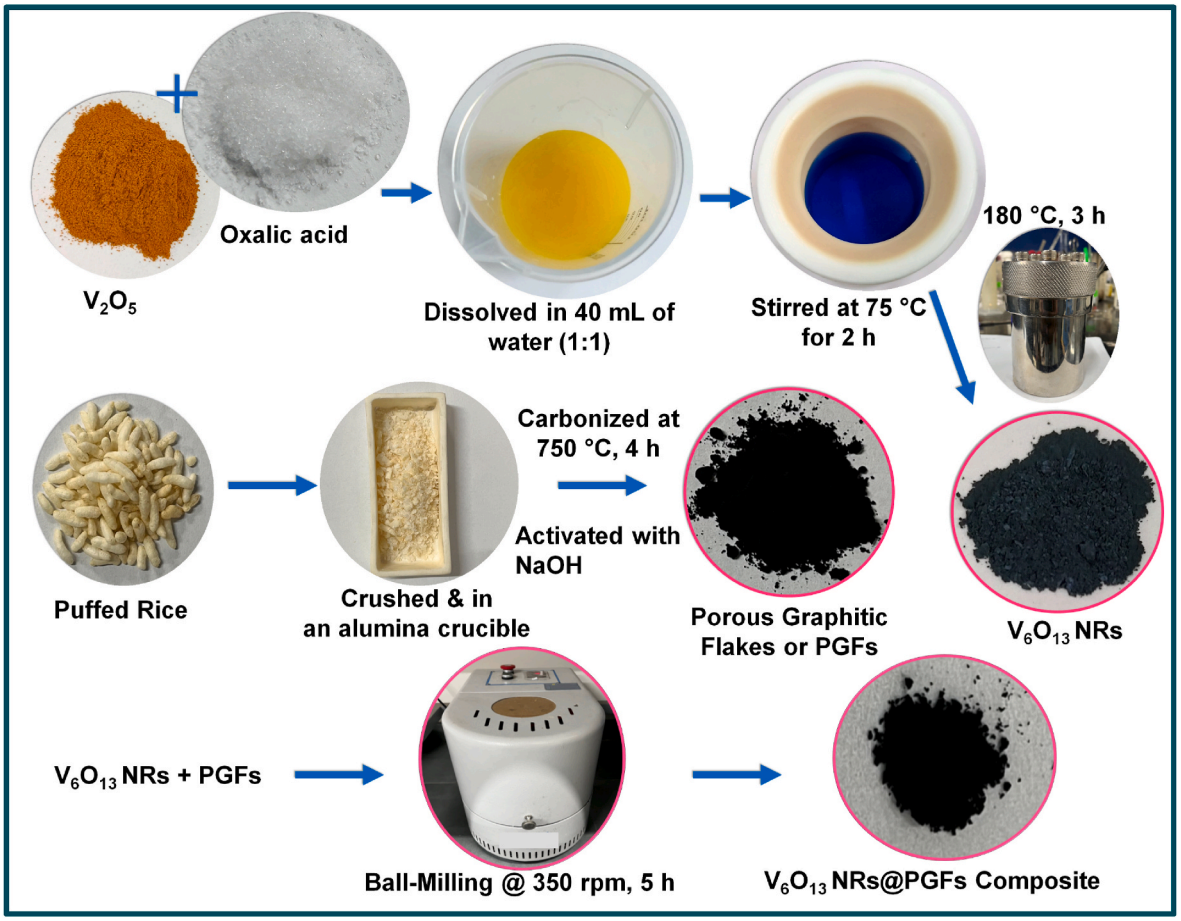

Scheme 1. Synthesis of V_6O_{13} NRs, PGFs and the V_6O_{13} NRs@PGFs composite.

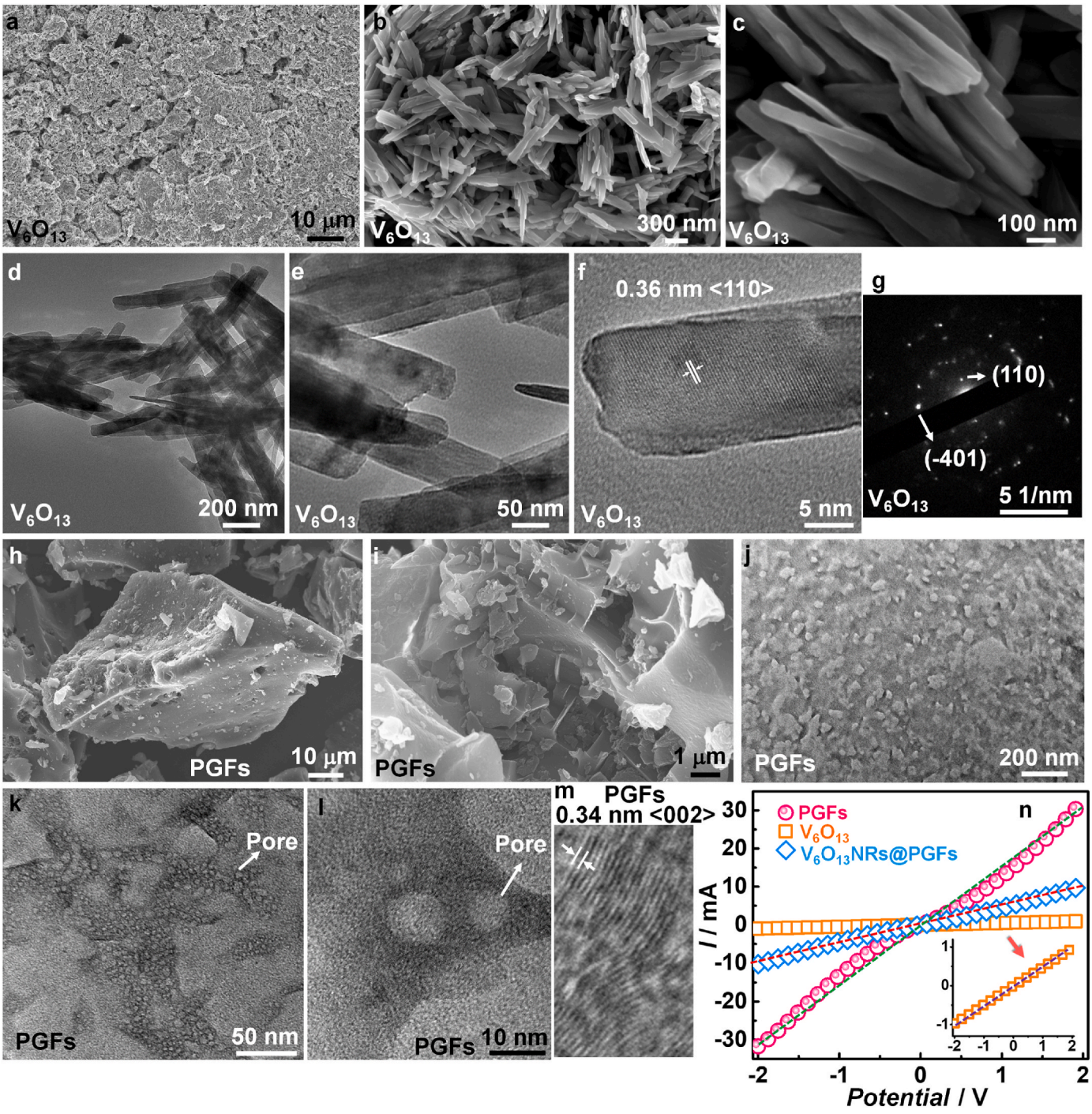

Fig. 1. (a-c) FE-SEM images and (d-f) TEM images of V_6O_{13} NRs and (g) SAED pattern of V_6O_{13} NRs. (h-j) FE-SEM images and (k-m) TEM images of PGFs. (n) I–V characteristics of V_6O_{13} NRs (enlarged view as an inset), PGFs and V_6O_{13} NRs@PGFs.

voids are present in between the rods, which is beneficial for the electrolyte to pass through, and enables accessing of the deeper recesses of the active electrode material during charge-discharge. This improves ion-adsorption and the subsequent Faradaic reaction. Compared to a previous report on Al/Ga co-doped V_6O_{13} nanorods where particles cum NRs were obtained, here only NRs are obtained [60]. TEM images also corroborate with the SEM observations. An interconnected network of smooth nanorods of V_6O_{13} are seen in the TEM images (Fig. 1d,c) as well with diameters of 50–60 nm. The nanorods offer one-dimensional pathways for charge (electron) transport thereby allowing fast charge transport across the cross section of the active material. This in turn can reduce the diffusion lengths for Zn^{2+} ions which results in fast electrochemical kinetics and improves rate capability. The high-resolution image of a nanorod (Fig. 1f) shows clear lattice fringes stacked in parallel. The inter-fringe distance is 0.36 nm and it matches with the (110) plane of monoclinic V_6O_{13}. The associated selected area electron diffraction (SAED) pattern in Fig. 1g shows bright spots superimposed over concentric rings. They are indexed to the (110) and (−401) planes (JCPDS: 43-1050). The pattern matches with that obtained previously for V_6O_{13} NRs prepared hydrothermally from V_2O_5 and oxalic acid precursors [41].

FE-SEM images of porous graphitic flakes (PGFs) (Fig. 1h–j) reveal

the irregular shaped bulky 3D particles of carbon with a flaky nature characterized by a large specific surface area. This allows anchoring of a high proportion of ions during charge-discharge. The high resolution TEM images (Fig. 1k,l) show the flakes to be mesoporous, with pores of 5–10 nm in dimensions. The porosity exhibited by this material is advantageous for buffering the volume expansion experienced by V_6O_{13} upon intercalation of Zn^{2+} ions in the oxide matrix. A lattice scale image in Fig. 1m shows slightly contorted fringes, with inter-fringe distance of 0.34 nm corresponding to the (002) plane of hexagonal graphite (JCPDS: 75-1621). The graphitic structure imparts good electrical conductivity to PGFs, which is also confirmed from its' I–V characteristics.

3.2. Electrical conduction behavior of cathode materials

Electrical conduction in the active cathode materials was studied from their I–V characteristics (Fig. 1n) The data was recorded in the LSV mode by sandwiching the sample between two stainless steel (SS) electrodes, over the voltage range −2 to +2 V at a scan rate of 20 mV s^{-1}. PGFs exhibit a sigmoidal I–V profile. Linear fitting of the curve over the part which shows linear dependence gave a conductivity (σ) of 14.6 mS cm^{-1}. It is determined from the relation: $\sigma = \left(\frac{1}{R}\right) \times \left(\frac{d}{a}\right)$. Here, 1/R is equal to the slope of the I–V curve (ΔI/ΔV), d is the cross-sectional thickness, and a is the exposed active area. PGFs are electrically conducting because of the graphitic carbon framework. In this structure, the carbons are present in a hexagonal arrangement. Three carbon atoms form sp^2 hybridized sigma bonds in the graphitic plane. The last non-hybridized (π)-electron is free to move above and below these planes, which is responsible for the high conductivity. The conductivity of pristine V_6O_{13} is 0.05 mS cm^{-1}, which is approximately 10^3 times lower than that of pure PGF. The proper mixing of V_6O_{13} and PGFs serves two purposes. (1) Conductivity of the composite increases, hence the rate performance also improves, due to rapid electron propagation in the composite compared to pure V_6O_{13}. (2) The volume expansion experienced by the oxide lattice during Zn^{2+} ion insertion also buffered by PGF. PGF accommodates the volume expansion of the oxide. Pristine V_6O_{13} has a nominal conductivity primarily due to the +5 and + 4 oxidation states of vanadium (V^{4+}/V^{5+}). Observed conductivity is due to the inter-valent charge transfer between two adjacent vanadiums (from site A to site B) present in the +4 and + 5 oxidation states.

$$V^{4+}\,(A) + V^{5+}\,(B) \rightarrow V^{5+}\,(A) + V^{4+}\,(B) \quad (1)$$

The V_6O_{13} NRs@PGFs composite is characterized by an electrical conductivity of 4.8 mS cm^{-1} which is 100 times higher in magnitude compared to that of pristine V_6O_{13}. This demonstrates the composite's suitability as a cathode for developing ZIBs with a good power density (besides the high energy density).

3.3. XRD and Raman studies of cathode materials

XRD patterns and Raman spectra of V_6O_{13} NRs and V_6O_{13} NRs@PGFs (3:1) composite are shown in Fig. 2. XRD pattern of pristine V_6O_{13} NRs (Fig. 2a) exhibits multiple intense peaks at 2θ = 25.3°, 28.3°, 30.1°, 33.5°, 38.3°, 45.6°, 49.5°, 53.9°, 59.8° and 69.6°. These peaks are indexed to the (110), ($\bar{2}$03), ($\bar{4}$01), ($\bar{3}$11), (113), ($\bar{6}$01), (020), ($\bar{6}$04), ($\bar{7}$11) and ($\bar{6}$21), planes of a monoclinic end centered V_6O_{13} structure with the C2/*m* space group (JCPDS: 43-1050). The pattern matches well with that reported for thin V_6O_{13} nanobelts grown by a hydrothermal route [44] and also with standard data [61]. These planes correspond to d-spacings of 3.5, 3.1, 3.0, 2.7, 2.3, 2.0, 1.8, 1.7, 1.5 and 1.3 Å. The data agrees well with the lattice scale imaging results. V_6O_{13} has a tunnel like structure where these elongated channels are created by alternating single and double layers composed of VO_6 units with shared corners. This structure provides ample sites for ion storage. While the double layers have both V^{5+} and V^{4+} sites, the single layers have only V^{5+} sites [62]. This open structure is conducive for facile Zn^{2+} ion movement is shown in a schematic in Scheme 2. The V_6O_{13} NRs@PGFs composite shows peaks pre-dominantly from V_6O_{13}. A few peaks have also been masked and found to be in lowered in intensity than pristine V_6O_{13}. This is possibly due to van der Waals or electrostatic interactions between V_6O_{13} NRs and PGFs. It also indicates a proper mixing of V_6O_{13} NRs and PGFs.

Raman spectrum of V_6O_{13} NRs (Fig. 2b) displays a highly intense peak at 141 cm^{-1} which has a B_g symmetry and other peaks with medium intensity at 283, 407, 520 and 689 cm^{-1}, which are assigned to the bending vibrations of V–O, V═O, three-coordinated O–V_3 bonds and the bridging V–O–V bonds. These assignments agree well with those reported for highly crystalline V_6O_{13} films grown by pulse laser deposition [63]. A sharp peak is observed at ~990 cm^{-1}, and this arises from the stretching vibrational modes of the terminal V═O bonds [64]. Raman

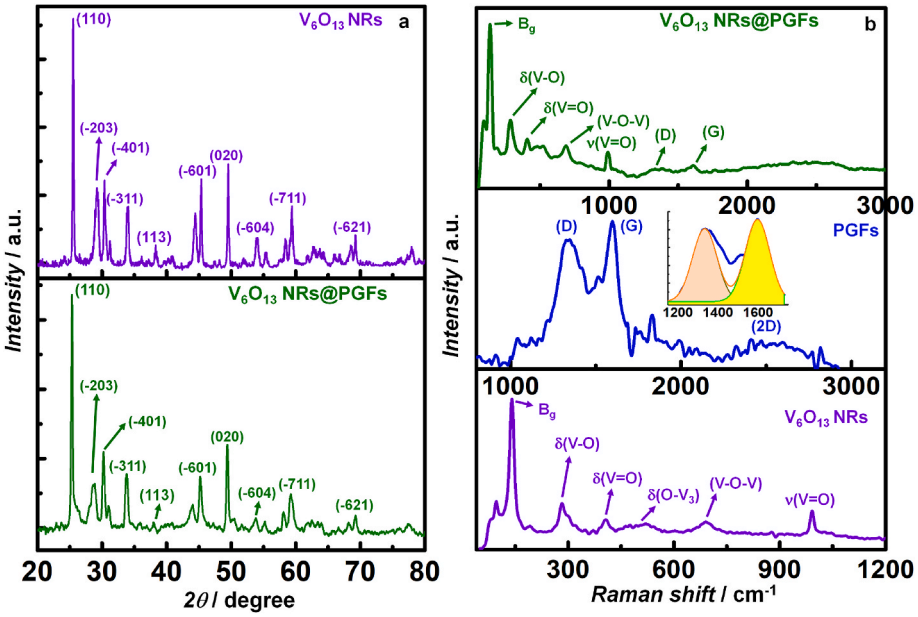

Fig. 2. (a) XRD patterns of V_6O_{13} NRs and V_6O_{13} NRs@PGFs composite and (b) Raman spectra of V_6O_{13} NRs, PGFs, V_6O_{13} NRs@PGFs composite. Inset in (b) represents the Gaussian fits for D/G bands.

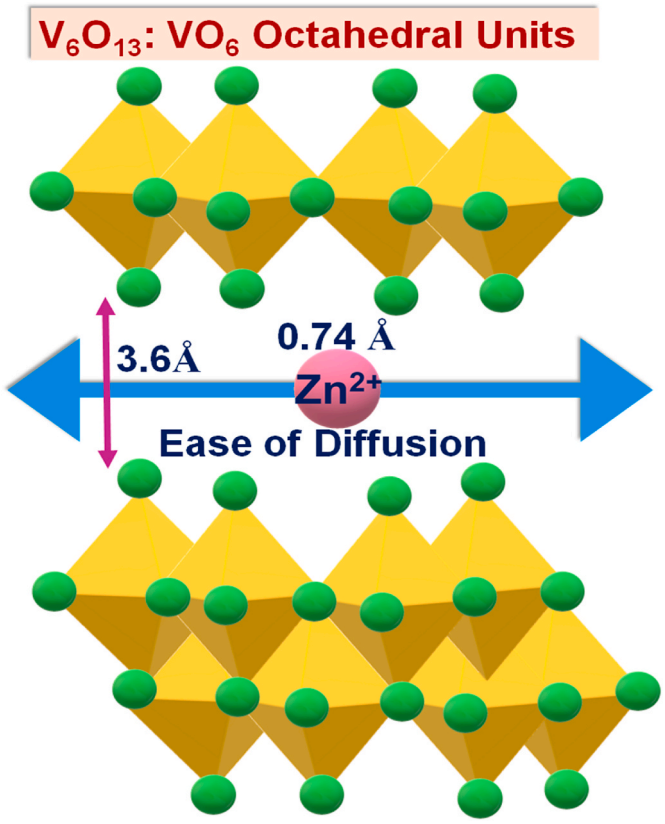

Scheme 2. Structure of V_6O_{13} NRs.

spectrum of PGFs, shows the D-band and the G-band at 1329 and 1595 cm^{-1} respectively. The D-band is attributed to the breathing mode of A_{1g} symmetry. The out-of-plane vibrations of structural defects (described as the oxygen functionalities covalently bonded to the sp^3 hybridized carbons). The G-band, has a E_{2g} symmetry. It is produced from the in-plane vibrations of sp^2 bonded carbon atoms in the graphitic layers or carbon chains. The I_D/I_G ratio is 0.96, suggestive of nearly similar concentration for defects and the ordered graphitic carbons. The defects are a consequence of the strong alkali (NaOH) treatment that carbon is subjected to, done for maximizing the porosity of the carbon matrix. This porosity is helpful for accommodating the volume expansion that V_6O_{13} undergoes during discharging, when Zn^{2+} ions diffuse through the oxide framework. The overtone of the fundamental D-vibration, i.e., the 2D mode is observed as a very broad hump centered at ~2590 cm^{-1}. The composite: V_6O_{13} NRs@PGFs is characterized by multiple peaks corresponding to the V–O vibrational modes of the oxide and the D-and G-bands of PGFs. The B_g and the δ(V–O) modes are blue-shifted to 136 and 278 cm^{-1} respectively, compared to the pristine oxide. This implies that interaction between the carbons and the oxide, weakens the V–O bond strengths.

3.4. Compositional features of V_6O_{13} NRs@PGFs composite

XPS survey spectrum for the V_6O_{13} NRs@PGFs composite shows intense and distinctive peaks due to different core levels of the constituent elements. They are: O2s (20.7 eV), V3p (41.6 eV), V3s (69.3 eV), C1s (284.6 eV), $V2p_{3/2}$ (517.0 eV), $V2p_{1/2}$ (525.0 eV), O1s (530.2 eV) and V2s (630.7 eV). While the "O"-peaks originate from the oxide and the PGFs, all the "V"-signals are attributed to V_6O_{13}. The V2p spectrum (Fig. 3b) exhibits a broad doublet due to the spin-orbital splitting components of $V2p_{1/2}$ and $V2p_{3/2}$ at ~ 524.6 and 517.5 eV. A similar set of twin peaks was also obtained for polycrystalline V_6O_{13} [65]. Each of these broad peaks is divided into two components due to V^{4+} and V^{5+}. This matches with a previous report on this oxide prepared from V_2O_5 [41]. As shown in the inset, the structure comprises of four of the vanadiums in the 4+ and two of them in the 5+ state, thus yielding a ratio of 2:1 for V^{4+}/V^{5+} in V_6O_{13}. The highly asymmetric O1s spectrum (Fig. 3c) is deconvoluted into three peaks at 531.9, 532.75 and 534.05 eV. They are assigned to V^{5+}-O, V^{4+}=O and C–O groups which aligns with the resolved V2p components.

The C1s peak (Fig. 3d) is resolved into three components at 286.3, 287.6 and 291.1 eV which are attributed to the C–C, C–O and the π-π* shake-up satellite peaks. The C–O peak arises from the oxygen containing functional groups (C–O–C, C–OH, $C–OH_2$, C═O) which are

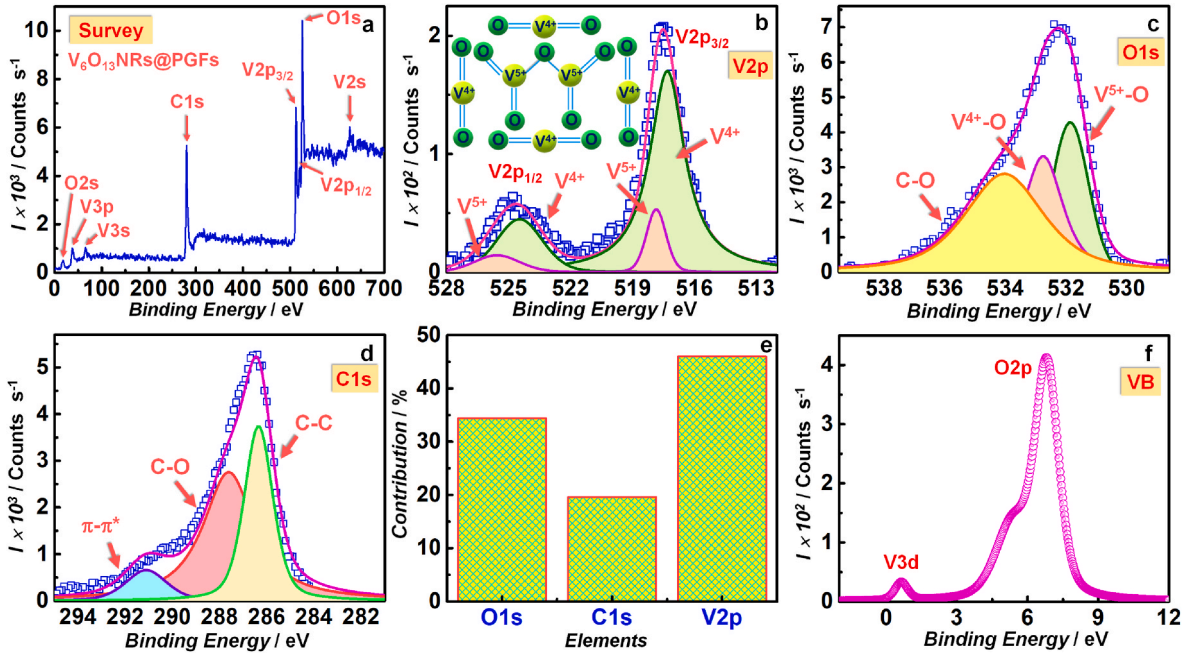

Fig. 3. XPS spectra: (a) survey spectrum, deconvoluted (b) V2p, (c) O1s and (d) C1s spectra, (e) % elemental contributions and (f) fitted VB spectrum of the V_6O_{13}@PGF composite.

integrated into the carbon framework during the PGF synthesis via alkali activation. The percentage mass contributions of the elements estimated from the core levels are 46.0% (V), 34.4% (O) and 19.6% (C) (Fig. 3e). The V:O atomic ratio is found to be 0.42. It is close to the expected ratio of 0.46, as per the stoichiometry of V_6O_{13}. The fitted VB spectrum in Fig. 3f, reveals two peaks due to the O2p and V3d levels. This is in agreement with a previously reported hard XPS data of V_6O_{13} that shows a broad highly intense asymmetric V2p band at 0.65 eV and a low intensity V3d peak at 0.5 eV [66]. The V3d band corresponds to the VB, for the density of states rapidly declines to zero close to 0 eV, which is the Fermi level. Assuming that E_F lies approximately at the mid-point of the band gap, the band gap is estimated to be approximately 1 eV. The narrow gap confirms the semiconducting nature of the oxide and is also indicative of its electrically conductive nature.

3.5. Electrochemical characteristics of ZIBs

Cyclic voltammetry (CV) and galvanostatic charge-discharge (GCD) plots were measured over the voltage range 0.2–2.0 V, versus Zn^{2+}/Zn, with the following ZIB cell architectures: pristine V_6O_{13} NRs//Zn (Cell type I), V_6O_{13} NRs@PGFs//Zn (Cell type II) and V_6O_{13} NRs@PGFs//PCz@CNTs@Zn (Cell type III). The nominal voltage of the three cells is the same, 1.8 V. The plots are displayed in Figs. 4 and 5. In the first two cases, the anode was pristine Zn metal foil. In the third case, the anode with a thin coating of PCz@CNTs composite was used. In all cases, a non-aqueous electrolyte of 0.5 M $Zn(CF_3SO_3)_2$ in acetonitrile was employed.

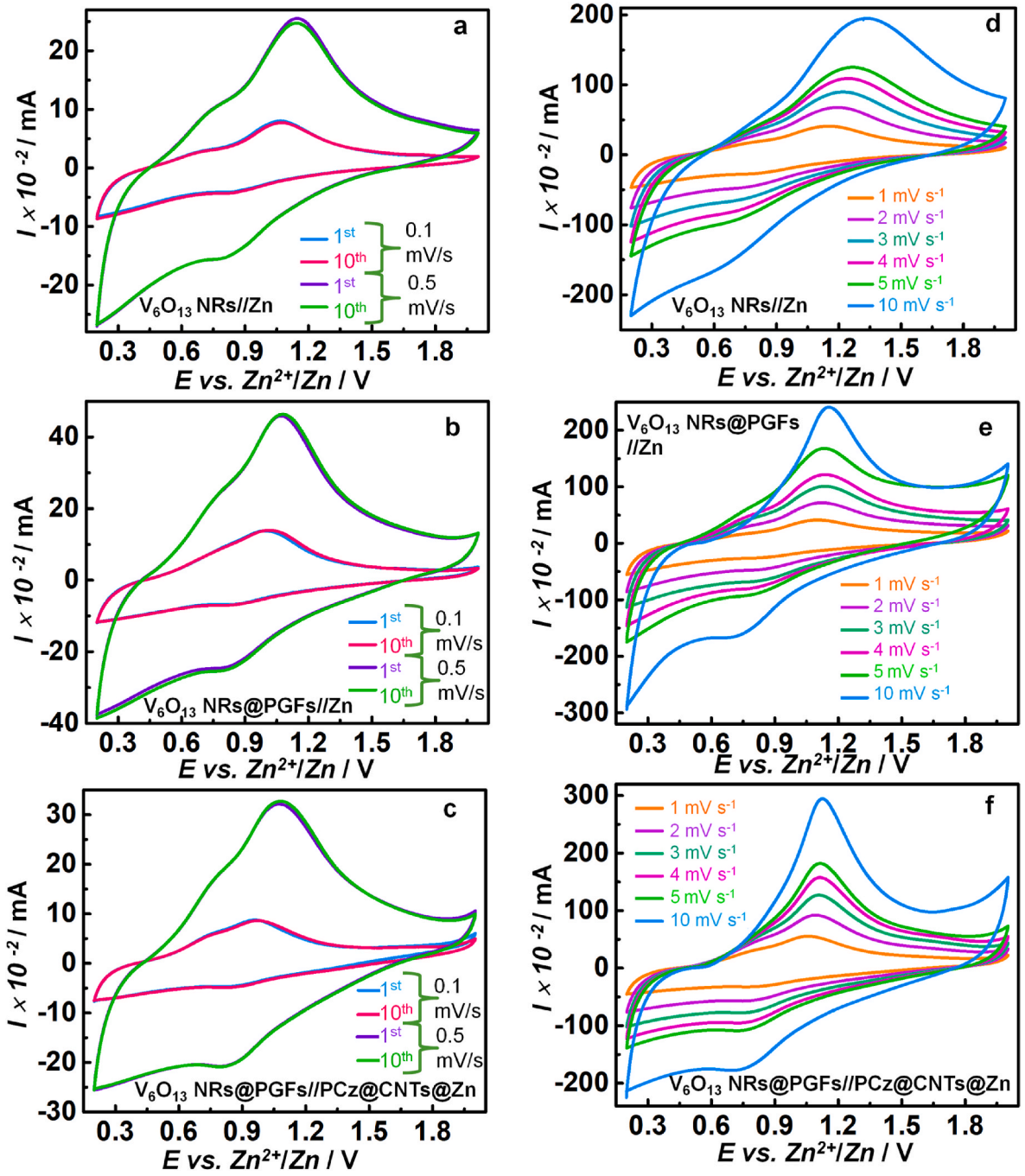

Fig. 4. CV plots of ZIBs with following cell architecture: V_6O_{13}//Zn, V_6O_{13} NRs@PGFs//Zn and V_6O_{13} NRs@PGFs//PCz@CNTs@Zn: (a-c) at 0.1 and 0.5 mV s^{-1}, (d-f) at different scan rates ranging from 1 to 10 mV s^{-1}.

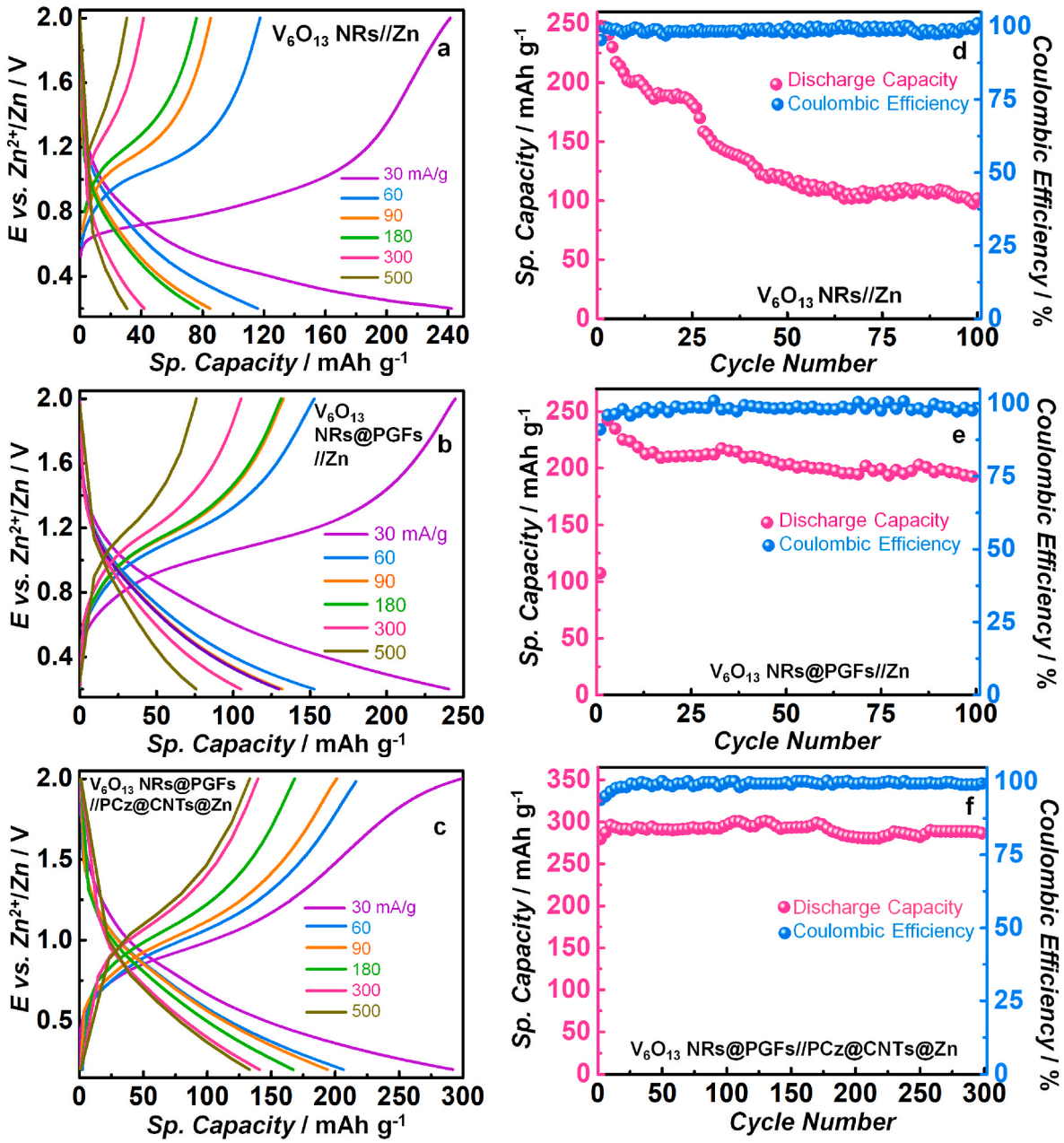

Fig. 5. ZIBs with following cell architectures: V_6O_{13} NRs//Zn, V_6O_{13} NRs@PGFs//Zn and V_6O_{13} NRs@PGFs//PCz@CNTs@Zn: (a-c) GCD plots at different current densities and (d-f) variation in specific capacity and Coulombic efficiency as a function of number of cycles at 30 mA g^{-1}.

The CV plots were recorded at both low (0.1 and 0.5 mV s^{-1}) (Fig. 4a,c,e) and high (1-5, 10 mV s^{-1}) scan rates (Fig. 4b,d,f). In the first cycle, at 0.1 mV s^{-1}, principal redox peaks (E_{red}/E_{ox}) are found at 0.83/1.06 V, 0.84/1.01 V and 0.84/0.96 V. At 0.5 mV s^{-1} redox peaks are observed at 0.80/1.14 V, 0.81/1.07 V and 0.82/1.07 V which signify the slight improvement in reversibility with nominal peak shift at high scan rates. The Zn^{2+} intercalation-deintercalation reactions are expressed through the equations below.

$$\text{Anode: } yZn \rightleftarrows yZn^{2+} + 2ye^{-} \quad (2)$$

$$\text{Cathode: } yZn^{2+} + V_6O_{13} + 2ye^{-} \rightleftarrows Zn_yV_6O_{13} \quad (3)$$

V_6O_{13} NRs@PGFs composite oxidizes at a reduced voltage due to superior electrical conductivity compared to pristine V_6O_{13} NRs. In the cell containing Zn anode with the PCz@CNTs composite coating, dendritic growth and dissolution have been reduced (as will be seen later) hence higher reversibility was achieved. CV plots recorded at higher scan rates (Fig. 4b,d,f) in the range of 1–10 mV s^{-1}, show peak flattening at high scan rates in the ZIB with pristine oxide, where the reduction peak was almost invisible at 10 mV s^{-1}. However, both oxidation and reduction peaks are prominently visible in the Cell type III.

In the GCD plots collected at various current densities for V_6O_{13} NRs (Fig. 5a,c,e) discharge and charge plateaus were observed at ~0.8 V and ~1.2 V. These concur well with the observed CV plots. In case of cell type I, the maximum discharge capacity was ~241 mAh g^{-1} at 30 mA g^{-1} and it decreased to ~30 mAh g^{-1} at 0.5 A g^{-1}. The poor electrical conductivity of pristine V_6O_{13}, does not allow fast electron transport at high current densities, and therefore rate performance declines due to sluggish kinetics. Furthermore, only 41% capacity retention was observed after 100 cycles. In case of Cell type II, a capacity of ~75 mAh g^{-1} at 0.5 A g^{-1} was achieved which further increased to ~133 mAh g^{-1} at 0.5 A g^{-1} with increment in capacity at low current density i.e., ~291

mAh g^{-1} at 30 mA g^{-1} for Cell type III. Capacity retentions were also improved to 80% and ~99% for the respective cells. Coulombic efficiency (CE) was found to vary between 93 and 99% for Cell types I and II. For Cell type III, CE was low in the initial few cycles due to the activation of electrodes, and after 30 cycles, it is high and stable at ~99%. The initial energy densities of the three cells (type I, II and III) are ~145, ~146 and ~175 Wh kg^{-1}. The power density of full cell or Cell type III is 18 W kg^{-1} and it is calculated using the following equation: P (W/kg) = I (mA/g) × V/Active electrode mass (mg). The V_6O_{13} NRs@PGFs//PCz@CNTs@Zn cell (or Cell type III) was cycled for 300 cycles at a current density of 30 mA g^{-1} (Fig. 5f). The initial discharge capacity was 291 mAh g^{-1} and the cell was able to retain ~98% of its initial capacity even after 300 cycles. At the end of 300 cycles, a capacity of 286 mAh g^{-1} was obtained. The excellent reversibility demonstrated by the cell is also reflected in the high CE (~94–99%) achieved over 300 cycles.

From rate capability plot (Fig. 6a) we get to know that the Cell type I retains only ~63% of fresh cells' highest discharge capacity when tested

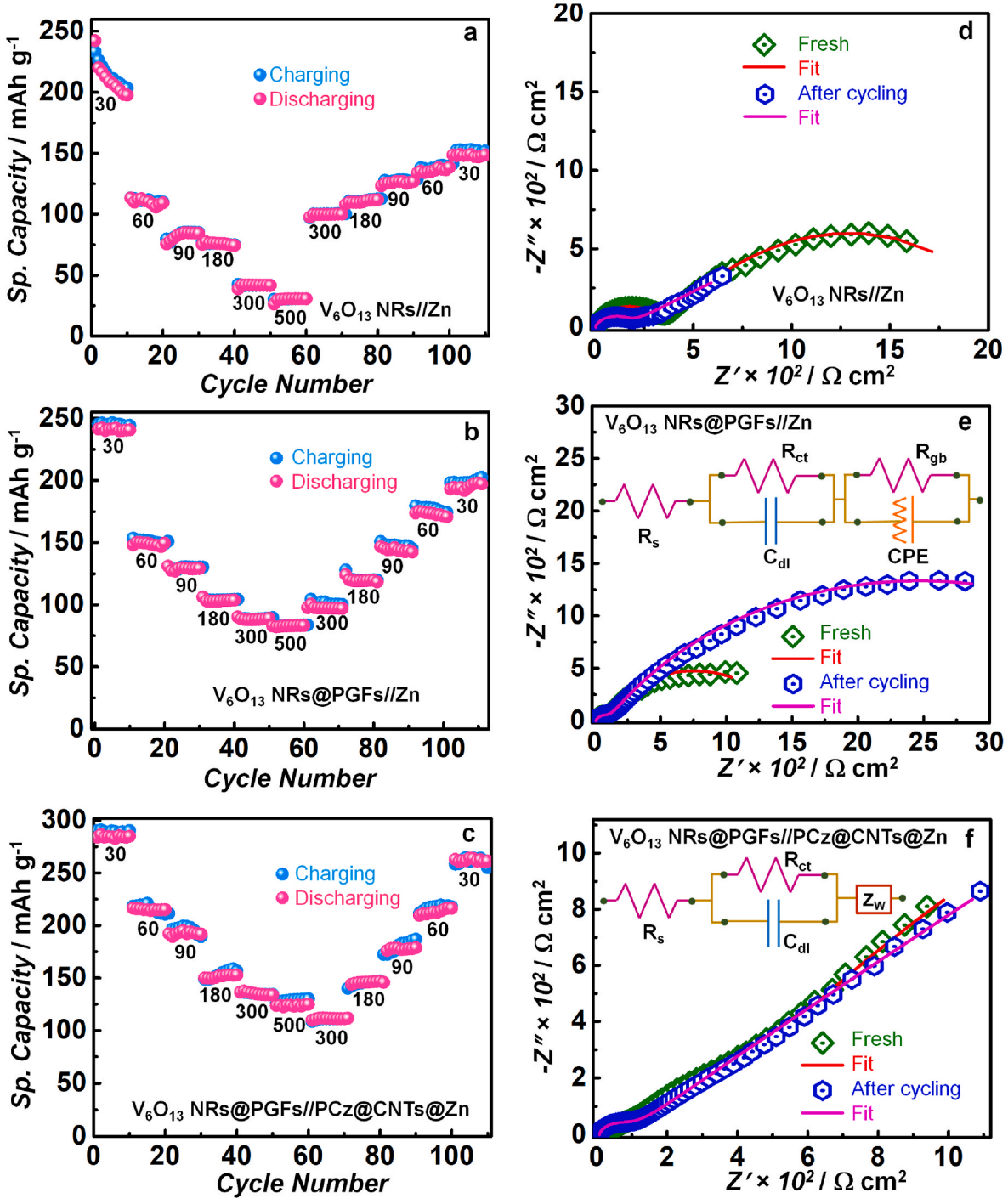

Fig. 6. ZIBs with following cell architecture: pristine V_6O_{13} NRs//Zn, V_6O_{13} NRs@PGFs//Zn and V_6O_{13} NRs@PGFs//PCz@CNTs@Zn: (a-c) rate capability curves, as a function of cycling and current densities. (d-f) Nyquist plots for the same ZIBs, before cycling, and after 100 charge-discharge cycles, recorded over a frequency range of 1 MHz to 0.01 Hz, under the open circuit potential, and an ac amplitude of 20 mV. Equivalent circuits used for fitting the plots in (d,e) and (f) are shown as insets of (e) and (f).

at 30 mA g^{-1} after 100 cycles of the initial run. The volume expansion and contraction of V_6O_{13}, during Zn^{2+} intercalation and deintercalation produces mechanical stresses in the material. To relieve this strain, the active material disintegrates slowly, dissipates into the electrolyte, thus resulting in capacity fade with cycling. This capacity retention has been improved in the Cell type II, where 70.5% of the fresh cells' capacity was retained at 30 mA g^{-1} (Fig. 6c). This improvement is ascribed to the presence of PGFs, which accommodate the volume expansion experienced by V_6O_{13}, but at the same time, this enhancement was also not very remarkable may be due the dendritic growth on anode surface. Although it is less than that observed in aqueous systems but still it is present. So, a further modification of the cell architecture is useful, especially in the view of developing long lasting ZIBs. A thin layer coating of PCz@CNTs composite was introduced on the Zn anode surface to reduce dendritic growth, as accomplished through Cell type III.

Conducting polymers like PCz are chemically robust and highly compatible with non-aqueous electrolytes like the zinc triflate/acetonitrile one, used here. Similarly, CNTs are again electrically conducting as well as inert (in terms of undergoing any side reactions with Zn) and facilitate fast charge transfer and reaction kinetics at the anode/electrolyte interface, which affords stable homogeneous deposition of Zn thereby forming a smooth deposit of Zn with no dendritic growth. About 92.5% fresh cells' capacity retention is achieved with Cell type III thus supporting our conjecture (Fig. 6e). Cell type III incorporates the benefits of both strategies: (1) inclusion of PGFs in the cathode to accommodate the volume variation of the active material and increase the conductivity for facile charge transportation. (2) PCz@CNTs composite coating on Zn-anode which reduces the dendritic growth. Hence improved capacity, rate performance and cycling life are achieved.

3.6. EIS studies on fresh and cycled ZIBs

Nyquist plots for fresh and cycled ZIBs are displayed in Fig. 6d–f. While the V_6O_{13} NRs//Zn and the V_6O_{13} NRs@PGFs//Zn cells exhibit two distorted arcs, the V_6O_{13} NRs@PGFs//PCz@CNTs@Zn cell shows a skewed semicircle followed by a straight line. The data for the cells with the Zn-anode (Cell types I and II) was fitted into a [R(RC)(RQ)] circuit. The cell with the PCz@CNTs@Zn anode (Cell type III) was fitted into a [R(RC)W] circuit. The salient fitted parameters are summarized in Table 1. The charge transfer resistance at the electrolyte/cathode interface is the least for Cell type III and highest for Cell type I. The PGFs in the cathode improve electron transfer and transport across the thickness of the V_6O_{13} NRs@PGFs, which in turn allows facile transfer of Zn^{2+} ions from the electrolyte. The ion-diffusion conductance is also high for Cell type III. With cycling there are only moderate changes observed in the impedance parameters, indicating that the cell cycles well.

Relevant storage data from different groups (mostly on ZIBs based on non-aqueous electrolytes, since the present work also uses a non-aqueous electrolyte) [67–76] is compared with the performance metrics obtained in our work in Fig. 7. It can be observed that our capacity values are superior to most of the reported data. This figure also demonstrates the efficacy of the cell configuration fabricated in this report for a stable durable ZIB.

Table 1
Fitting parameters for Nyquist plots of different ZIBs.

Cell configuration	R_s (Ω cm^2)	R_{ct} (Ω cm^2)	C_{dl} (F cm^{-2})	Y_o (mS $s^{1/2}$ cm^{-2})
V_6O_{13} NRs//Zn Fresh)	5	340	7	0.01
V_6O_{13} NRs//Zn (Cycled)	4	206	129	0.01
V_6O_{13} NRs@PGFs//Zn (Fresh)	5	113	931	2.80
V_6O_{13} NRs@PGFs//Zn (Cycled)	9	129	149	0.05
V_6O_{13} NRs@PGFs// PCz@CNTs@Zn (Fresh)	6	64	9	2.30
V_6O_{13} NRs@PGFs// PCz@CNTs@Zn (Cycled)	7	103	1	1.05

3.7. Morphological aspects and structure of PCz, CNTs and PCz@CNTs composite

The anode coating is composed of a composite of poly(carbazole) and multiwalled carbon nanotubes (PCz@CNTs). The polymer (Fig. 8a and b) is characterized by a closely packed network of interlinked cauliflower like shapes and agrees well with the morphology reported in literature [77]. The FTIR spectrum of PCz (Fig. 8c) confirms the polymer formation for characteristic peaks at the following positions: 3407 cm^{-1} due to the stretching vibrations of the N–H bond in the PCz chains, 1451 cm^{-1} due to the C–C stretching mode (the carbons from two adjacent monomers) and implying the conversion of monomer units into the polymer chains, ~1650 cm^{-1} due to the C═C stretching mode and 1290 cm^{-1} due to the ν(C–N) stretching vibrational mode are observed and they roughly match with the reported spectra [78,79]. A strong peak at 748 cm^{-1} arises from the N–H deformation mode, and a broad one at 579 cm^{-1} is attributed to the C═C out of plane twisting vibrations [77]. The slight variations in comparison to literature is possibly due to different polymer chain lengths and dopants.

The CNTs are constituted by bundles of continuous interconnected aggregated nanotubes which appear like furry shapes with a good uniformity that extends over multiple microns (Fig. 8d and e). Ion microscopy image in Fig. 8f, reveals the thickness of the tubes to be in the range of 25–40 nm, and the image of the PCz@CNTs composite (Fig. 8g) reveals the globular polymer particles to be enmeshed with the tubular structures of CNTs, indicative of a good mixing of the two components. The sheet resistance of pristine uncoated Zn anode is ~0.5 Ω cm^{-2}. After coating the anode with a thin layer of the PCz@CNTs composite, it is ~4.5 Ω cm^{-2}. This indicates that the electrical conductivity of the metal anode remains largely unaltered by the polymer/CNT coating. The photographs of pristine Zn anode and the same coated with PCz@CNTs, before and after long term cycling are shown in Fig. 8h. It is observed that while the PCz@CNTs@Zn anode's physical appearance changes very slightly with cycling. But the Zn anode undergoes a substantial change from a smooth surface to one with deposits, suggestive of the effectiveness of the polymer/CNT coating in protecting the Zn surface from dendrite formation. These are further characterized by AFM in the next section.

The XRD patterns of the fresh and the cycled V_6O_{13} NRs@PGFs composite electrodes are shown in Fig. 9a. Some peaks from monoclinic V_6O_{13} are retained in the cycled electrode, albeit lowered intensities and broadened peak widths. The loss in crystallinity originates from the repetitive insertion and extraction of Zn^{2+} ions, which causes the slow amorphisation of the cathode. The FE-SEM images of the uncycled V_6O_{13} NRs@PGFs composite (Fig. 9b and c) show the nanorods from the oxide and the carbon microstructures to be mixed well. Post-cycling, the composite exhibits a fuzzy texture wherein the contours of the oxide nanorods and the flaky structures of carbon are visible in the images (Fig. 9d and e). The composite retains its structure even after cycling highlighting that it has a robust structure and can endure repeated cycling well, which is also confirmed from the nominal capacity fade. The composite retains ~99% of its initial capacity. In contrast, pristine V_6O_{13} is unable to sustain extended cycling, which is reflected in the dramatic capacity fade, which occurs by 41%.

3.8. Impact of cycling on Zn versus PCz@CNTs@Zn anodes

The effect of cycling on pristine Zn anode and PCz@CNTs@Zn anode can be gauged from their AFM images, which are shown in Fig. 9f–i. Pristine uncycled Zn anode (Fig. 9f) has a smooth surface and the root mean square surface roughness (R_{rms}) is about 7 nm. However, after cycling (Fig. 9g), the growth of the metallic Zn dendrites is clearly perceptible on the Zn surface (extracted from Cell type II). The dendrites

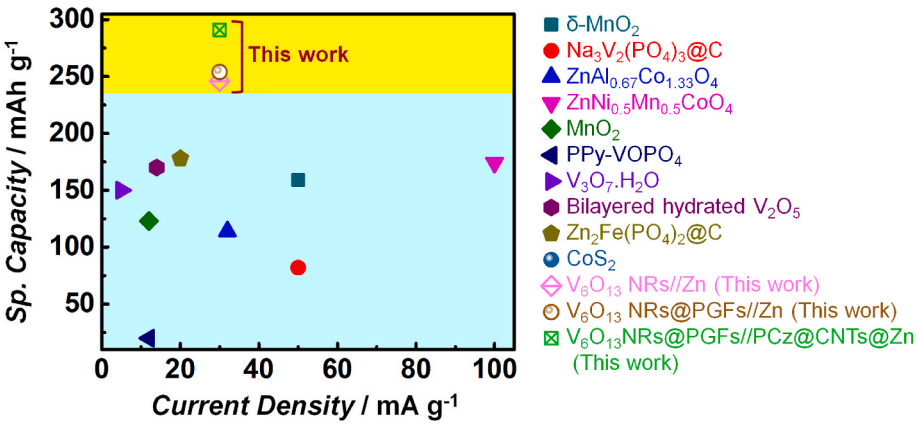

Fig. 7. Comparison of capacity of ZIBs from literature with that of the ZIBs fabricated in this work.

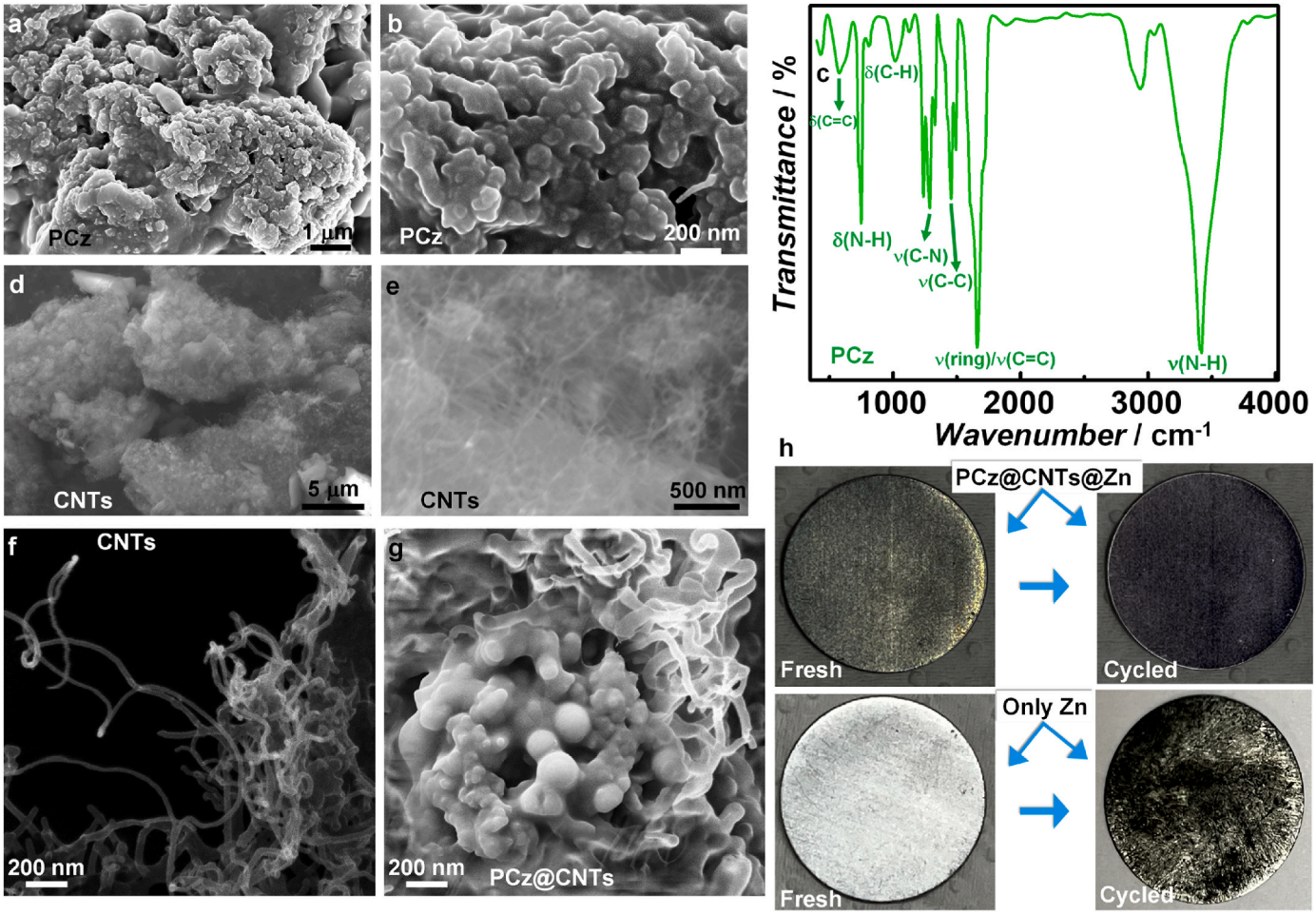

Fig. 8. (a,b) FE-SEM images and (c) FTIR spectrum of PCz, (d,e) FE-SEM images of MWCNTs and ion microscopy images of (f) MWCNTs and (g) PCz@CNTs composite. (h) Photographs of fresh and cycled Zn and PCz@CNTs@Zn anodes.

are formed during the charging process, when Zn^{2+} ions reduce at the anode, and deposit over the surface in the form of dendrites. The rms roughness also drastically rises to about ~522 nm. Dendrites can eventually lead to short circuit and even fires. They can also induce capacity loss, by undergoing Zn loss via decomposition reactions with the electrolyte. The effectiveness of the PCz@CNTs coating in inhibiting dendrite growth is evident from the topography images of the fresh and cycled PCz@CNTs@Zn anode (Fig. 9h and i) extracted from Cell type III.

XRD patterns of fresh and cycled anodes of Zn and PCz@CNTs@Zn are shown in Fig. S1. Fresh Zn anode is highly crystalline. The XRD pattern exhibits multiple strong and intense peaks at $2\theta = 36.25^{o}$, 38.94^{o}, 43.12^{o}, 54.17^{o}, 69.88^{o}, 70.62^{o} and 80.04^{o}. These are assigned to the (002), (100), (101), (102), (103), (110) and (004) planes of the hexagonal crystal structure of Zn, according to JCPDS card: 03-065-5973. This pattern matches with that obtained for hexagonal Zn platelets in an earlier report [80]. After cycling, the intensity of the (002) peak corresponding to an inter-planar spacing of 0.25 nm is reduced by 63%. Besides the (002) peak, all the remaining peaks except the (100)

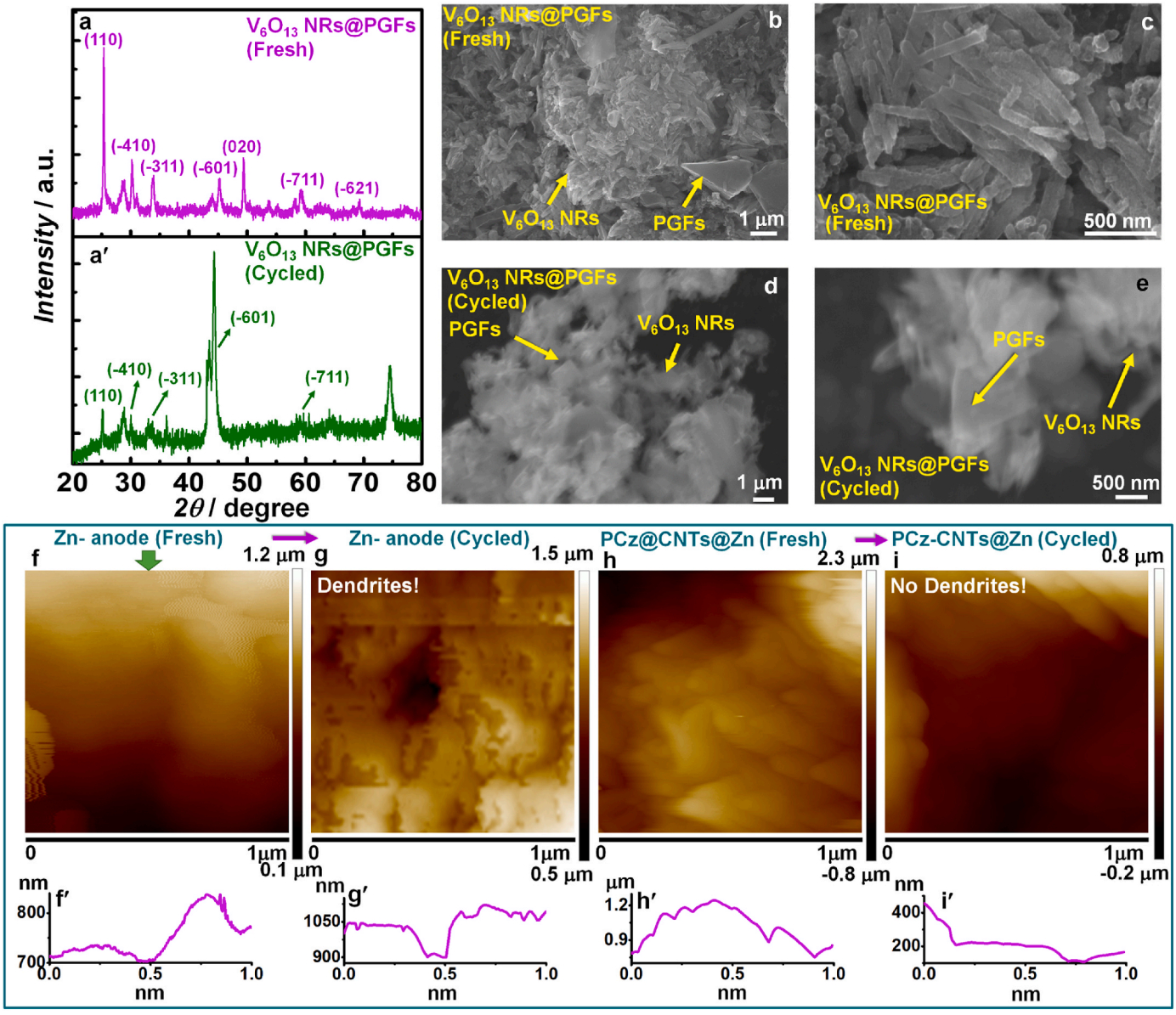

Fig. 9. (a) XRD patterns and (b-e) FE-SEM images of fresh and cycled V_6O_{13} NRs@PGFs electrode. AFM topography images of (f) fresh and (g) cycled Zn anode and (h) fresh and (i) cycled PCz@CNTs@Zn anode and their corresponding section profiles (f′-i′).

peak also exhibit small intensity losses with cycling. This represents the effect of the plated Zn deposit over the Zn surface during cycling. During the charging cycle, Zn^{2+} ions migrate from the cathode, pass through the electrolyte and undergo reduction at the Zn surface, and this is called "plated Zn". This Zn is then stripped during the discharge cycle via oxidation and they diffuse to the cathode. The dendritic shapes of plated Zn cause this change in the XRD pattern. Fresh PCz@CNTs@Zn anode also shows a pattern similar to that of fresh Zn albeit a lowered intensity for the (002) peak. The very high crystallinity of Zn obscures the contributions from PCz and CNTs, which generally give very weak peaks. Post cycling, for this anode, surprisingly there are some intensity enhancements indicating that the plated Zn growth has a morphology different from that obtained over pristine Zn surface. This is further confirmed from SEM analysis.

The cross-sectional FE-SEM images of the cycled Zn anode, fresh and cycled PCz@CNTs coated Zn electrodes are shown in Fig. 10. The growth of elongated Zn dendrites on the surface of the Zn anode is clearly visible in Fig. 10a. Zn dendrites are formed due to the uneven deposition of Zn during the charging cycle. Zinc deposition commences with nucleation and once a Zn nucleus is formed, the subsequent Zn^{2+} ions prefer to deposit over the nucleus for it is energetically more favorable, as opposed to deposition over the available free Zn surface [81]. The length of the Zn dendrites is about 10–11 μm. Previously fern like Zn-dendrites of length of about 60 μm in aqueous systems have been reported [82]. Here the length is shorter, due to the use of a non-aqueous electrolyte. The cross-sectional view of the fresh PCz@CNTs@Zn electrode (Fig. 10b) shows the presence of the globular polymer particles mingling with the tubular CNT structures. A good homogeneous mixing of the two components is achieved. The microstructure is highly porous which enables facile Zn^{2+} ion diffusion across the thickness of the composite coating during charging process. Unlike the uncoated Zn surface, here, Zn^{2+} ions can diffuse uniformly through the pores of the composite and then deposit evenly over the Zn surface (Fig. 10c). At the PCz@CNTs/Zn interface, the reduced Zn deposit is distinctly observed. The observed thickness is about ~2 μm, and above this height, it is possible that the plated Zn is obscured by the polymer and the nanotubes. A magnified view shows the porous matrix which the composite affords, allows the percolation of Zn^{2+} ions and inhibits dendritic growth (Fig. 10d).

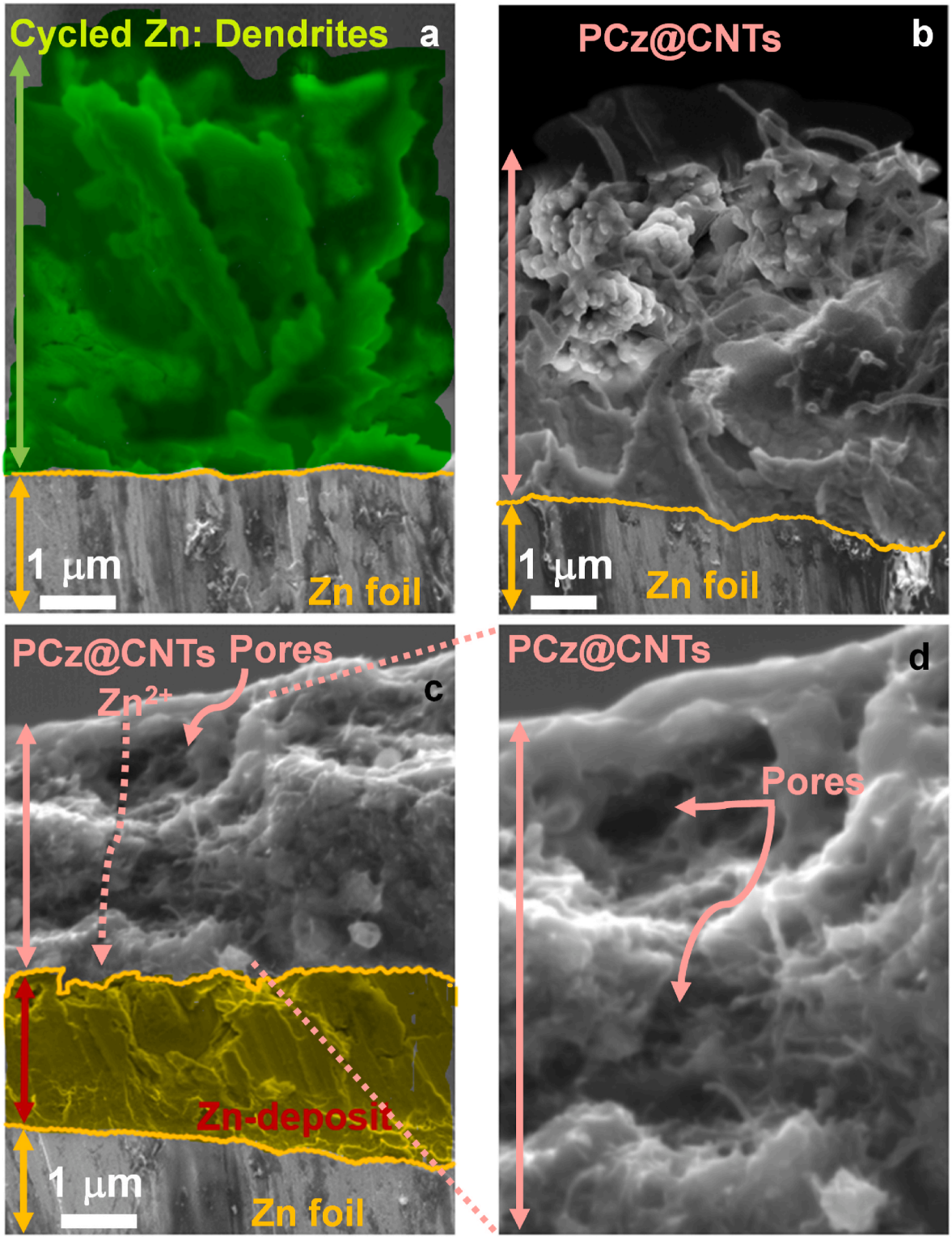

Fig. 10. (a) Cycled Zn anode, (b) fresh- and (c) cycled- PCz@CNTs@Zn electrodes; magnified view of the composite from (c) is shown in (d). Plated Zn and dendrite growth have been color-labelled in yellow and green. (For interpretation of the references to color in this figure legend, the reader is referred to the Web version of this article.)

An electrically conducting composite overlayer at anode has the following benefits. During the charging process for uniform Zn deposition at the anode, the high electrical conductivity of the PCz@CNTs composite allows the uniform conduction of electrons from the Zn surface across the thickness of the composite. These electrons are accepted by the incoming Zn^{2+} ions and facile Zn reduction occurs at the electroactive sites present at surface of the composite. This results in a uniform plating of Zn and inhibits dendritic growth [83]. This is also supported by the small rms roughness change. It increases from ~72 to ~96 nm ongoing from the uncycled to the cycled electrode.

3.9. Extended cycling of cell type III

Another cell with the same configuration was also subjected to 1500 charge-discharge cycles at a high current density of 300 mA g^{-1} (Fig. S2). About 100% capacity retention was achieved at a high current density of 300 mA g^{-1} and after 1500 cycles a discharge capacity of ~135 mAh g^{-1} with Cell type III was retained (Fig. S2c). This suggests that even when the cell is operated under fast kinetic conditions, it can retain a high capacity, which does not reduce with cycling. Both the cathode and the anode materials preserve their structural integrities with repetitive Zn^{2+} ion insertion and extraction and do not pulverize or detach from the current collector thus resulting in the high capacity as well as its' retention with cycling. In the initial cycles, the capacity value is less, but through repetitive cycling, utilization of active material by intercalation/deintercalation process as well as capacity increases. The CV plot shows only a small decrement of anodic as well as cathodic peak currents. Slight peak shifts were also observed due to some side reaction inside the cell. Topography map in Fig. S2a shows that there are still no signs of dendrite formation on the modified Zn anode, indicating that the PCz@CNTs composite overlayer is highly effective in restricting the growth of fiber-like Zn. The capacity fade also is nominal, indicating that the V_6O_{13} NRs@PGFs cathode is able to preserve its' structural integrity with cycling. Furthermore, as CE also continues to be high (93–99%) in the cycled ZIB, it is evident that there is no irreversible Zn^{2+} ion trapping in the cathode or any inactive Zn deposition at the anode.

4. Conclusions

One of the most formidable issues that adversely affects the long-term cycling ability of aqueous ZIBs is the progressive growth of dendrites at the Zn anode. In this work, a composite layer of PCz@CNTs is found to be highly effective in supressing the dendritic growth. This overlayer is electrically conducting and allows facile transfer of electrons to the vicinal Zn^{2+} ions during the charging cycle and enables their non-fiber like deposition at the Zn surface. Compositionally, being a conducting polymer/CNTs hybrid, the layer is also electrochemically and chemically robust and endures long-term cycling exceptionally well. Besides the anode modification, a V_6O_{13} NRs@PGFs cathode was used, where the layered nanostructure of the oxide affords short ion-diffusion pathways and the presence of conducting PGFs (which in turn were derived from a cheap agricultural produce, namely, puffed rice) improves the rate kinetics of Zn^{2+} ion-intercalation at high current densities. PGFs due to their mesoporous structure permit deep and uniform percolation of electrolyte species thereby enhancing the reactive site/ion interactions. PGFs also serve as cushion to offset the strain experienced via volume expansion by V_6O_{13} NRs by repetitive Zn^{2+} ion insertion and extraction, thus enhancing cycling lifespan. The post-cycling capacities after 100 cycles for the following non-aqueous ZIBs: V_6O_{13} NRs//Zn, and V_6O_{13} NRs@PGFs//Zn are ~102 and ~193 mAh g^{-1} at 30 mA g^{-1} and energy densities are ~61 and ~116 Wh kg^{-1} respectively, with capacity retentions of 42% and 79% respectively. Dendrite formation plagues the un-modified Zn anode, whereas the PCz@CNTs coated Zn anode is completely dendrite free. After prolonged cycling, i.e., 300 cycles, the V_6O_{13} NRs@PGFs//PCz@CNTs@Zn cell delivers a capacity of ~286 mAh g^{-1} (at 30 mA g^{-1}) and after 1500 cycles, a capacity of ~124 mAh g^{-1} at 300 mA g^{-1} is achieved. The ZIB with the modified anode experiences minimal capacity fade and continues to be dendrite free, clearly demonstrating the efficacy of this simple approach of deploying a PCz@CNTs overlayer for durable long lasting non-aqueous metal ion batteries with stable energy storage performances.

Author statement

Souvik Naskar: Investigation, Resources, Writing-Original Draft. **Manoranjan Ojha:** Investigation. **Tapu Raihan Gazi:** Investigation. **Partha Ghosal:** Investigation. **Melepurath Deepa:** Conceptualization, Supervision, Project administration, Funding acquisition.

Declaration of competing interest

The authors declare that they have no known competing financial interests or personal relationships that could have appeared to influence the work reported in this paper.

Data availability

Data will be made available on request.

Acknowledgements

Financial support for this work from Science & Engineering Research Board (SERB) of India (Grant no. CRG/2020/000482) is gratefully acknowledged by M. Deepa, S. Naskar and M. Ojha. S.N. is thankful to CSIR for the grant of junior research fellowship.

Appendix A. Supplementary data

Supplementary data to this article can be found online at https://doi.org/10.1016/j.compositesb.2023.110516.

References

[1] Wen J, Yu Y, Chen C. A review on lithium-ion batteries safety issues: existing problems and possible solutions. Mater Exp 2012;2:197–212. https://doi.org/10.1166/mex.2012.1075.
[2] Sun Y, Shi P, Xiang H, Liang X, Yu Y. High-safety nonaqueous electrolytes and interphases for sodium-ion batteries. Small 2019;15:1805479. https://doi.org/10.1002/smll.201805479.
[3] Massé RC, Uchaker E, Cao G. Beyond Li-ion: electrode materials for sodium- and magnesium-ion batteries. Sci China Mater 2015;58:715–66. https://doi.org/10.1007/s40843-015-0084-8.
[4] Das SK, Mahapatra S, Lahan H. Aluminium-ion batteries: developments and challenges. J Mater Chem A 2017;5:6347–67. https://doi.org/10.1039/C7TA00228A.
[5] Song M, Tan H, Chao D, Fan HJ. Recent advances in Zn-ion batteries. Adv Funct Mater 2018;28:1802564. https://doi.org/10.1002/adfm.201802564.
[6] Zhu C, Ma Y, Zang W, Guan C, Liu X, Pennycook SJ, Wang J, Huang W. Conformal dispersed cobalt nanoparticles in hollow carbon nanotube arrays for flexible Zn-air and Al-air batteries. J Chem Eng 2019;369:988–95. https://doi.org/10.1016/j.cej.2019.03.147.
[7] Song Z, Zhang G, Deng X, Zou K, Xiao X, Momen R, Massoudi A, Deng W, Hu J, Hou H, Zou G, Ji X. Ultra-low-dose pre-metallation strategy served for commercial metal-ion capacitors. Nano-Micro Lett 2022;14:53. https://doi.org/10.1007/s40820-022-00792-x.
[8] Deng X, Zou K, Momen R, Cai P, Chen J, Hou H, Zou G, Ji X. High content anion (S/Se/P) doping assisted by defect engineering with fast charge transfer kinetics for high-performance sodium ion capacitors. Sci Bull 2021;66:1858–68. https://doi.org/10.1016/j.scib.2021.04.042.
[9] Song Z, Zhang G, Deng X, Tian Y, Xiao X, Deng W, Hou H, Zou G, Ji X. Strongly coupled interfacial engineering inspired by robotic arms enable high-performance sodium-ion capacitors. Adv Funct Mater 2022;32:2205453. https://doi.org/10.1002/adfm.202205453.
[10] Liang H, Shi R, Zhou Y, Jiang W, Sun T, Zhang Z, Sun L, Lian J, Li H, Bu Y. Removing cost barriers to template carbon synthesis for high-performance supercapacitors by establishing a zero-emission chemical cycle from CO_2. ACS Energy Lett 2022:4381–8. https://doi.org/10.1021/acsenergylett.2c02203.
[11] Durmus YE, Zhang H, Baakes F, Desmaizieres G, Hayun H, Yang L, Kolek M, Küpers V, Janek J, Mandler D, Passerini S, Ein-Eli Y. Side by side battery technologies with lithium-ion based batteries. Adv Energy Mater 2020;10:2000089. https://doi.org/10.1002/aenm.202000089.
[12] Tang B, Shan L, Liang S, Zhou J. Issues and opportunities facing aqueous zinc-ion batteries. Energy Environ Sci 2019;12:3288–304. https://doi.org/10.1039/C9EE02526J.
[13] Konarov A, Voronina N, Jo JH, Bakenov Z, Sun Y-K, Myung S-T. Present and future perspective on electrode materials for rechargeable zinc-ion batteries. ACS Energy Lett 2018;3:2620–40. https://doi.org/10.1021/acsenergylett.8b01552.
[14] Zhang Y, Deng S, Li Y, Liu B, Pan G, Liu Q, Wang X, Xia X, Tu J. Anchoring MnO_2 on nitrogen-doped porous carbon nanosheets as flexible arrays cathodes for advanced rechargeable Zn–MnO_2 batteries. Energy Storage Mater 2020;29:52–9. https://doi.org/10.1016/j.ensm.2020.04.003.
[15] Zhang Y, Deng S, Pan G, Zhang H, Liu B, Wang X-L, Zheng X, Liu Q, Wang X, Xia X, Tu J. Introducing oxygen defects into phosphate ions intercalated manganese

dioxide/vertical multilayer graphene arrays to boost flexible zinc ion storage. Small Methods 2020;4:1900828. https://doi.org/10.1002/smtd.201900828.
[16] He P, Chen Q, Yan M, Xu X, Zhou L, Mai L, Nan C-W. Building better zinc-ion batteries: a materials perspective. J Energy Chem 2019;1:100022. https://doi.org/10.1016/j.enchem.2019.100022.
[17] Wan F, Niu Z. Design strategies for vanadium-based aqueous zinc-ion batteries. Angew Chem Int Ed 2019;131:16508–17. https://doi.org/10.1002/ange.201903941.
[18] Yu P, Zeng Y, Zhang H, Yu M, Tong Y, Lu X. Flexible Zn-ion batteries: recent progresses and challenges. Small 2019;15:1804760. https://doi.org/10.1002/smll.201804760.
[19] Blanc LE, Kundu D, Nazar LF. Scientific challenges for the implementation of Zn-ion batteries. Joule 2020;4:771–99. https://doi.org/10.1016/j.joule.2020.03.002.
[20] Gao J, Xie X, Liang S, Lu B, Zhou J. Inorganic colloidal electrolyte for highly robust zinc-ion batteries. Nano-Micro Lett 2021;13:69. https://doi.org/10.1007/s40820-021-00595-6.
[21] Zhang N, Chen X, Yu M, Niu Z, Cheng F, Chen J. Materials chemistry for rechargeable zinc-ion batteries. Chem Soc Rev 2020;49:4203–19. https://doi.org/10.1039/C9CS00349E.
[22] Wang P, Shi X, Wu Z, Guo S, Zhou J, Liang S. Layered hydrated vanadium oxide as highly reversible intercalation cathode for aqueous Zn-ion batteries. Carbon Energy 2020;2:294–301. https://doi.org/10.1002/cey2.39.
[23] Pang Q, Sun C, Yu Y, Zhao K, Zhang Z, Voyles PM, Chen G, Wei Y, Wang X. $H_2V_3O_8$ nanowire/graphene electrodes for aqueous rechargeable zinc ion batteries with high rate capability and large capacity. Adv Energy Mater 2018;8:1800144. https://doi.org/10.1002/aenm.201800144.
[24] Alfaruqi MH, Mathew V, Song J, Kim S, Islam S, Pham DT, Jo J, Kim S, Baboo JP, Xiu Z, Lee K-S, Sun Y-K, Kim J. Electrochemical zinc intercalation in lithium vanadium oxide: a high-capacity zinc-ion battery cathode. Chem Mater 2017;29:1684–94. https://doi.org/10.1021/acs.chemmater.6b05092.
[25] He P, Zhang G, Liao X, Yan M, Xu X, An Q, Liu J, Mai L. Sodium ion stabilized vanadium oxide nanowire cathode for high-performance zinc-ion batteries. Adv Energy Mater 2018;8:1702463. https://doi.org/10.1002/aenm.201702463.
[26] Cai Y, Liu F, Luo Z, Fang G, Zhou J, Pan A, Liang S. Pilotaxitic $Na_{1.1}V_3O_{7.9}$ nanoribbons/graphene as high-performance sodium ion battery and aqueous zinc ion battery cathode. Energy Storage Mater 2018;13:168–74. https://doi.org/10.1016/j.ensm.2018.01.009.
[27] Hu P, Zhu T, Wang X, Wei X, Yan M, Li J, Luo W, Yang W, Zhang W, Zhou L, Zhou Z, Mai L. Highly durable $Na_2V_6O_{16}{\cdot}1.63H_2O$ nanowire cathode for aqueous zinc-ion battery. Nano Lett 2018;18:1758–63. https://doi.org/10.1021/acs.nanolett.7b04889.
[28] Yang Y, Tang Y, Fang G, Shan L, Guo J, Zhang W, Wang C, Wang L, Zhou J, Liang S. Li_+ intercalated $V_2O_5 \cdot nH_2O$ with enlarged layer spacing and fast ion diffusion as an aqueous zinc-ion battery cathode. Energy Environ Sci 2018;11:3157–62. https://doi.org/10.1039/C8EE01651H.
[29] Wan F, Zhang L, Dai X, Wang X, Niu Z, Chen J. Aqueous rechargeable zinc/sodium vanadate batteries with enhanced performance from simultaneous insertion of dual carriers. Nat Commun 2018;9:1656. https://doi.org/10.1038/s41467-018-04060-8.
[30] Tang B, Fang G, Zhou J, Wang L, Lei Y, Wang C, Lin T, Tang Y, Liang S. Potassium vanadates WIth stable structure and fast ion diffusion channel as cathode for rechargeable aqueous zinc-ion batteries. Nano Energy 2018;51:579–87. https://doi.org/10.1016/j.nanoen.2018.07.014.
[31] Xia C, Guo J, Li P, Zhang X, Alshareef HN. Highly stable aqueous zinc-ion storage using a layered calcium vanadium oxide bronze cathode. Angew Chem Int Ed 2018;57:3943–8. https://doi.org/10.1002/anie.201713291.
[32] Ming F, Liang H, Lei Y, Kandambeth S, Eddaoudi M, Alshareef HN. Layered $Mg_xV_2O_5{\cdot}nH_2O$ as cathode material for high-performance aqueous zinc ion batteries. ACS Energy Lett 2018;3:2602–9. https://doi.org/10.1021/acsenergylett.8b01423.
[33] Xia C, Guo J, Lei Y, Liang H, Zhao C, Alshareef HN. Rechargeable aqueous zinc-ion battery based on porous framework zinc pyrovanadate intercalation cathode. Adv Mater 2018;30:1705580. https://doi.org/10.1002/adma.201705580.
[34] Sambandam B, Soundharrajan V, Kim S, Alfaruqi MH, Jo J, Kim S, Mathew V, Sun Y, Kim J. Aqueous rechargeable Zn-ion batteries: an imperishable and high-energy $Zn_2V_2O_7$ nanowire cathode through intercalation regulation. J Mater Chem A 2018;6:3850–6. https://doi.org/10.1039/C7TA11237H.
[35] Yan M, He P, Chen Y, Wang S, Wei Q, Zhao K, Xu X, An Q, Shuang Y, Shao Y, Mueller KT, Mai L, Liu J, Yang J. Water-lubricated intercalation in $V_2O_5{\cdot}nH_2O$ for high-capacity and high-rate aqueous rechargeable zinc batteries. Adv Mater 2018;30:1703725. https://doi.org/10.1002/adma.201703725.
[36] Hu P, Yan M, Zhu T, Wang X, Wei X, Li J, Zhou L, Li Z, Chen L, Mai L. Zn/V_2O_5 aqueous hybrid-ion battery with high voltage platform and long cycle life. ACS Appl Mater Interfaces 2017;9:42717–22. https://doi.org/10.1021/acsami.7b13110.
[37] Kundu D, Adams BD, Duffort V, Vajargah SH, Nazar LF. A high-capacity and long-life aqueous rechargeable zinc battery using a metal oxide intercalation cathode. Nat Energy 2016;1:1–8. https://doi.org/10.1038/nenergy.2016.119.
[38] He J, Liu X, Zhang H, Yang Z, Shi X, Liu Q, Lu X. Enhancing Zn-ion storage capability of hydrated vanadium pentoxide by the strategic introduction of La^{3+}. ChemSusChem 2020;13:1568–74. https://doi.org/10.1002/cssc.201902659.
[39] Liu N, Wu X, Fan L, Gong S, Guo Z, Chen A, Zhao C, Mao Y, Zhang N, Sun K. Intercalation pseudocapacitive Zn^{2+} storage with hydrated vanadium dioxide toward ultrahigh rate performance. Adv Mater 2020;32:1908420. https://doi.org/10.1002/adma.201908420.
[40] Wang Y, Zhou L, Cao X, Gao X, Lu X. Promoting Zn^{2+} storage capability of a vanadium-based cathode via structural reconstruction for aqueous Zn-ion batteries. J Mater Chem A 2021;9:26698–703. https://doi.org/10.1039/D1TA08305H.
[41] Shi W, Yin B, Yang Y, Sullivan MB, Wang J, Zhang Y-W, Yu ZG, Lee WSV, Xue J. Unravelling V_6O_{13} diffusion pathways via CO_2 modification for high-performance zinc ion battery cathode. ACS Nano 2021;15:1273–81. https://doi.org/10.1021/acsnano.0c08432.
[42] Lai J, Zhu H, Zhu X, Koritala H, Wang Y. Interlayer-expanded $V_6O_{13}{\cdot}nH_2O$ architecture constructed for an advanced rechargeable aqueous zinc-ion battery. ACS Appl Energy Mater 2019;2:1988–96. https://doi.org/10.1021/acsaem.8b02054.
[43] Liu Y-Y, Yuan G-Q, Wang X-Y, Liu J-P, Zeng Q-Y, Guo X-T, Wang H, Liu C-S, Pang H. Tuning electronic structure of ultrathin V_6O_{13} nanobelts via nickel doping for aqueous zinc-ion battery cathodes. Chem Eng J 2022;428:132538. https://doi.org/10.1016/j.cej.2021.132538.
[44] Tamilselvan M, Sreekanth TVM, Yoo K, Kim J. Binder-free coaxially grown V_6O_{13} nanobelts on carbon cloth as cathodes for highly reversible aqueous zinc ion batteries. Appl Surf Sci 2020;529:147077. https://doi.org/10.1016/j.apsusc.2020.147077.
[45] Hu J, Chen H, Xiang K, Xiao L, Chen W, Liao H, Chen H. Preparation for V_6O_{13}@ Hollow carbon microspheres and their remarkable electrochemical performance for aqueous zinc-ion batteries. J Alloys Compd 2021;856:157085. https://doi.org/10.1016/j.jallcom.2020.157085.
[46] Lin Y, Zhou F, Xie M, Zhang S, Deng C. $V_6O_{13-}\delta$@C nanoscrolls with expanded distances between adjacent shells as a high-performance cathode for a knittable zinc-ion battery. ChemSusChem 2020;13:3696–706. https://doi.org/10.1002/cssc.202000699.
[47] Zhang Q, Luan J, Tang Y, Ji X, Wang S, Wang H. A facile annealing strategy for achieving in situ controllable Cu_2O nanoparticle decorated copper foil as a current collector for stable lithium metal anodes. J Mater Chem A 2018;6:18444–8. https://doi.org/10.1039/C8TA07612J.
[48] Sagane F, Ikeda K, Okita K, Sano H, Sakaebe H, Iriyama Y. Effects of current densities on the lithium plating morphology at a lithium phosphorus oxynitride glass electrolyte/copper thin film interface. J Power Sources 2013;233:34–42. https://doi.org/10.1016/j.jpowsour.2013.01.051.
[49] Zeng Y, Zhang X, Qin R, Liu X, Fang P, Zheng D, Tong Y, Lu X. Dendrite-free zinc deposition induced by multifunctional CNT frameworks for stable flexible Zn-ion batteries. Adv Mater 2019;31:1903675. https://doi.org/10.1002/adma.201903675.
[50] Zhang Q, Luan J, Fu L, Wu S, Tang Y, Ji X, Wang H. The three-dimensional dendrite-free zinc anode on a copper mesh with a zinc-oriented polyacrylamide electrolyte additive. Angew Chem 2019;131:15988–94. https://doi.org/10.1002/ange.201907830.
[51] Yin Y, Wang S, Zhang Q, Song Y, Chang N, Pan Y, Zhang H, Li X. Dendrite-free zinc deposition induced by tin-modified multifunctional 3D host for stable zinc-based flow battery. Adv Mater 2020;32:1906803. https://doi.org/10.1002/adma.201906803.
[52] Cao Q, Pan Z, Gao Y, Pu J, Fu G, Cheng G, Guan C. Stable imprinted zincophilic Zn anodes with high capacity. Adv Funct Mater 2022;32:2205771. https://doi.org/10.1002/adfm.202205771.
[53] Kang L, Cui M, Jiang F, Gao Y, Luo H, Liu J, Liang W, Zhi C. Nanoporous $CaCO_3$ coatings enabled uniform Zn stripping/plating for long-life zinc rechargeable aqueous batteries. Adv Energy Mater 2018;8:1801090. https://doi.org/10.1002/aenm.201801090.
[54] Liang P, Yi J, Liu X, Wu K, Wang Z, Cui J, Liu Y, Wang Y, Xia Y, Zhang J. Highly reversible Zn anode enabled by controllable formation of nucleation sites for Zn-based batteries. Adv Funct Mater 2020;30:1908528. https://doi.org/10.1002/adfm.201908528.
[55] Wang D, Fan Z, Zhou D, Khesro A, Murakami S, Feteira A, Zhao Q, Tan X, Reaney IM. Bismuth ferrite-based lead-free ceramics and multilayers with high recoverable energy density. J Mater Chem A 2018;6:4133–44. https://doi.org/10.1039/C7TA09857J.
[56] Zhao Z, Zhao J, Hu Z, Li J, Li J, Zhang Y, Wang C, Cui G. Long-life and deeply rechargeable aqueous Zn anodes enabled by a multifunctional brightener-inspired interphase. Energy Environ Sci 2019;12:1938–49. https://doi.org/10.1039/C9EE00596J.
[57] Li C, Liu S, Shi C, Liang G, Lu Z, Fu R, Wu D. Two-dimensional molecular brush-functionalized porous bilayer composite separators toward ultrastable high-current density lithium metal anodes. Nat Commun 2019;10:1363. https://doi.org/10.1038/s41467-019-09211-z.
[58] Cao Q, Gao H, Gao Y, Yang J, Li C, Pu J, Du J, Yang J, Cai D, Pan Z, Guan C, Huang W. Regulating dendrite-free zinc deposition by 3D zincopilic nitrogen-doped vertical graphene for high-performance flexible Zn-ion batteries. Adv Funct Mater 2021;31:2103922. https://doi.org/10.1002/adfm.202103922.
[59] Zhuo Y, Du C, Li X, Sun W, Chu Y. One-step synthesis and photoluminescence properties of polycarbazole spheres and Ag/polycarbazole core/shell composites. Eur Polym J 2013;49:1365–72. https://doi.org/10.1016/j.eurpolymj.2013.02.022.
[60] Zhang S, Zou Z, Zhang H, Liu J, Zhong S. Al/Ga co-doped V_6O_{13} nanorods with high discharge specific capacity as cathode materials for lithium-ion batteries. J Electroanal Chem 2021;890:115220. https://doi.org/10.1016/j.jelechem.2021.115220.
[61] Jain A, Ong SP, Hautier G, Chen W, Richards WD, Dacek S, Cholia S, Gunter D, Skinner D, Ceder G, Persson KA. Commentary: the materials Project: a materials genome approach to accelerating materials innovation. Apl Mater 2013;1:011002. https://doi.org/10.1063/1.4812323.

[62] Shan L, Zhou J, Zhang W, Xia C, Guo S, Ma X, Fang G, Wu X, Liang S. Highly reversible phase transition endows V_6O_{13} with enhanced performance as aqueous zinc-ion battery cathode. Energy Technol 2019;7:1900022. https://doi.org/10.1002/ente.201900022.

[63] Vijay VS, Varghese R, Sakunthala A, Rajesh S, Vidhya B. Highly crystalline V_2O_5 and V_6O_{13} thin films by PLD and a study on morphology transition of V_2O_5 by post annealing. Vacuum 2021;187:110097. https://doi.org/10.1016/j.vacuum.2021.110097.

[64] Velmurugan R, Premkumar J, Pitchai R, Ulaganathan M, Subramanian B. Robust, flexible, and binder free highly crystalline V2O5 thin film electrodes and their superior supercapacitor performances. ACS Sustainable Chem Eng 2019;7:13115–26. https://doi.org/10.1021/acssuschemeng.9b02302.

[65] Mendialdua J, Casanova R, Barbaux Y. XPS studies of V_2O_5, V_6O_{13}, VO_2 and V_2O_3. J Electron Spectrosc Relat Phenom 1995;71:249–61. https://doi.org/10.1016/0368-2048(94)02291-7.

[66] Suga S, Sekiyama A, Obara M, Yamaguchi J, Kimura M, Fujiwara H, Irizawa A, Yoshimura K, Yabashi M, Tamasaku K, Higashiya A, Ishikawa T. Hard X-ray photoelectron spectroscopy of metal–insulator transition in V_6O_{13}. J Phys Soc Japan 2010;79:044713. https://doi.org/10.1143/JPSJ.79.044713.

[67] Kao-ian W, Nguyen MT, Yonezawa T, Pornprasertsuk R, Qin J, Siwamogsatham S, Kheawhom S. Highly stable rechargeable zinc-ion battery using dimethyl sulfoxide electrolyte. Mater Today Energy 2021;21:100738. https://doi.org/10.1016/j.mtener.2021.100738.

[68] Li Q, Ma K, Hong C, Yang G, Wang C. Realizing excellent cycle stability of Zn/Na3V2(PO4)3 batteries by suppressing dissolution and structural degradation in non-aqueous Na/Zn dual-salt electrolytes. Sci China Mater 2021;64:1386–95. https://doi.org/10.1007/s40843-020-1550-2.

[69] Pan C, Nuzzo RG, Gewirth AA. $ZnAl_xCo_{2-x}O_4$ spinels as cathode materials for non-aqueous Zn batteries with an open circuit voltage of $\leq$2 V. Chem Mater 2017;29:9351–9. https://doi.org/10.1021/acs.chemmater.7b03340.

[70] Pan C, Zhang R, Nuzzo RG, Gewirth AA. $ZnNi_xMn_xCo_{2-2x}O_4$ spinel as a high-voltage and high-capacity cathode material for nonaqueous Zn-ion batteries. Adv Energy Mater 2018;8:1800589. https://doi.org/10.1002/aenm.201800589.

[71] Han S-D, Kim S, Li D, Petkov V, Yoo HD, Phillips PJ, Wang H, Kim JJ, More KL, Key B, Klie RF, Cabana J, Stamenkovic VR, Fister TT, Markovic NM, Burrell AK, Tepavcevic S, Vaughey JT. Mechanism of Zn insertion into nanostructured δ-MnO2: a nonaqueous rechargeable Zn metal battery. Chem Mater 2017;29:4874–84. https://doi.org/10.1021/acs.chemmater.7b00852.

[72] Verma V, Kumar S, Manalastas Jr W, Zhao J, Chua R, Meng S, Kidkhunthod P, Srinivasan M. Layered $VOPO_4$ as a cathode material for rechargeable zinc-ion battery: effect of polypyrrole intercalation in the host and water concentration in the electrolyte. ACS Appl Energy Mater 2019;2:8667–74. https://doi.org/10.1021/acsaem.9b01632.

[73] Kundu D, Vajargah SH, Wan L, Adams B, Prendergast D, Nazar LF. Aqueous vs. nonaqueous Zn-ion batteries: consequences of the desolvation penalty at the interface. Energy Environ Sci 2018;11:881–92. https://doi.org/10.1039/C8EE00378E.

[74] Senguttuvan P, Han S-D, Kim S, Lipson AL, Tepavcevic S, Fister TT, Bloom ID, Burrell AK, Johnson CS. A high power rechargeable nonaqueous multivalent Zn/V_2O_5 battery. Adv Energy Mater 2016;6:1600826. https://doi.org/10.1002/aenm.201600826.

[75] Zhou L-F, Gao X-W, Du T, Gong H, Liu L-Y, Luo W-B. New phosphate $Zn_2Fe(PO_4)_2$ cathode material for nonaqueous zinc ion batteries with long life span. ACS Appl Mater Interfaces 2022;14:8888–95. https://doi.org/10.1021/acsami.1c10380.

[76] Zhang R, Pan C, Nuzzo RG, Gewirth AA. CoS_2 as a sulfur redox-active cathode material for high-capacity nonaqueous Zn batteries. J Phys Chem C 2019;123:8740–5. https://doi.org/10.1021/acs.jpcc.9b02142.

[77] Baig U, Wani WA, Hun LT. Facile synthesis of an electrically conductive polycarbazole–zirconium(IV)phosphate cation exchange nanocomposite and its room temperature ammonia sensing performance. New J Chem 2015;39:6882–91. https://doi.org/10.1039/C5NJ01029B.

[78] Das M, Roy S. Preparation, characterization and properties of newly synthesized SnO_2-polycarbazole nanocomposite via room temperature solution phase synthesis process. Mater Today Proc 2019;18:5438–46. https://doi.org/10.1016/j.matpr.2019.07.573.

[79] Gupta B, Prakash R. Interfacial polymerization of carbazole: morphology controlled synthesis. Synth Met 2010;160:523–8. https://doi.org/10.1016/j.synthmet.2009.11.014.

[80] Mai NT, Thuy TT, Mott DM, Maenosono S. Chemical synthesis of blue-emitting metallic zinc nano-hexagons. CrystEngComm 2013;15:6606–10. https://doi.org/10.1039/C3CE40801A.

[81] Zuo Y, Wang K, Pei P, Wei M, Liu X, Xiao Y, Zhang P. Zinc dendrite growth and inhibition strategies. Mater Today Energy 2021;20:100692. https://doi.org/10.1016/j.mtener.2021.100692.

[82] Biton M, Tariq F, Yufit V, Chen Z, Brandon N. Integrating multi-length scale high resolution 3D imaging and modelling in the characterisation and identification of mechanical failure sites in electrochemical dendrites. Acta Mater 2017;141:39–46. https://doi.org/10.1016/j.actamat.2017.09.008.

[83] Kong X, Rudnicki PE, Choudhury S, Bao Z, Qin J. Dendrite suppression by a polymer coating: a coarse-grained molecular study. Adv Funct Mater 2020;30:1910138. https://doi.org/10.1002/adfm.201910138.